Stardust in STARDUST - the C, N, and O isotopic compositions of Wild 2 cometary matter in Al foil impacts

Frank J. Stadermann[1*], Peter Hoppe[2], Christine Floss[1], Philipp R. Heck[2], Friedrich Hörz[3], Joachim Huth[2], Anton T. Kearsley[4], Jan Leitner[5], Kuljeet K. Marhas[1], Kevin D. McKeegan[6], and Thomas Stephan[5]

[1]Laboratory for Space Sciences and Physics Department,
Washington University, St. Louis, Missouri 63130, USA

[2]Max Planck Institute for Chemistry, Particle Chemistry Department,
P.O. Box 3060, 55020 Mainz, Germany

[3]ARES, NASA Johnson Space Center, Houston, TX 77058, USA

[4]Department of Mineralogy, The Natural History Museum, London SW7 5BD, UK

[5]Institut für Planetologie, Westfälische Wilhelms-Universität Münster,
Wilhelm-Klemm-Str. 10, 48149 Münster, Germany

[6]Dept. of Earth and Space Sciences, University of California Los Angeles,
Los Angeles, CA 90095, USA

[*] Corresponding author. E-mail: fjs@wuphys.wustl.edu

submitted to
Meteoritics & Planetary Science

ABSTRACT

In January 2006, the STARDUST mission successfully returned dust samples from the tail of comet 81P/Wild 2 in two principal collection media, low density silica aerogel and Al foil. While hypervelocity impacts at 6.1 km/s, the encounter velocity of STARDUST, into Al foils are generally highly disruptive for natural, silicate-dominated impactors, previous studies have shown that many craters retain sufficient residue to allow a determination of the elemental and isotopic compositions of the original projectile. We have used the NanoSIMS to perform C, N, and O isotope imaging measurements on four large (59 – 370 μm diameter) and on 47 small (0.32 – 1.9 μm diameter) Al foil impact craters as part of the STARDUST Preliminary Examination. Most analyzed residues in and around these craters are isotopically normal (solar) in their C, N, and O isotopic compositions. However, the debris in one large crater shows an average ^{15}N enrichment of ~450 ‰, which is similar to the bulk composition of some isotopically primitive interplanetary dust particles. A 250 nm grain in another large crater has an ^{17}O enrichment with ~2.65 times the solar ^{17}O/^{16}O ratio. Such an O isotopic composition is typical for circumstellar oxide or silicate grains from red giant or asymptotic giant branch stars. The discovery of this circumstellar grain clearly establishes that there is authentic 'stardust' in the cometary samples returned by the STARDUST mission. However, the low apparent abundance of circumstellar grains in Wild 2 samples and the preponderance of isotopically normal material indicates that the cometary matter is a diverse assemblage of presolar and solar system materials.

INTRODUCTION

Isotopic studies of extraterrestrial matter can provide unique insights into a sample's origin and history. Despite widespread homogenization in the turbulent solar nebula, various vestiges of spatial and temporal heterogeneity during disk evolution (Boss 2004) allowed the preservation of isotopically anomalous matter that can now be found in primitive solar system materials, such as meteorites and interplanetary dust particles (IDPs). Such samples contain an isotopic memory of their presolar origins or of early solar system processes. The most extreme isotopic variations are found in sub-micrometer to micrometer sized circumstellar grains that survived interstellar transport and incorporation into the solar nebula as well as prolonged residencies in small solar system parent bodies (e.g., Zinner 2004). Other isotopic signatures in primitive solar system materials provide evidence about interstellar cloud chemistry (Zinner 1988; Messenger et al. 2003b; Floss et al. 2004; Busemann et al. 2006) and the formation condition for the earliest solar system materials (Scott and Krot 2005). The abundances and distributions of these isotopic markers in various types of extraterrestrial matter are highly variable and represent crucial indicators of a parent body's provenance and of the extent of secondary processing.

Short period comets originating in the Kuiper Belt ought to provide ideal conditions for the preservation of primitive materials from the early days of our solar system. These comets formed in the cold outer regions of the solar nebula at 5 to 50 AU and are thought to have remained cold enough throughout their history for incorporated interstellar grains to survive basically unaltered (Hanner 2003). A subgroup of the low inclination short period comets, the Jupiter-family comets, eventually find their way into the inner solar system where sublimation limits their average lifetime to an astronomically short ~12,000 years (Levison and Duncan 1997). One of these Jupiter-family comets is 81P/Wild 2, which had a close encounter with

Jupiter in September 1974 when it was deflected into a highly elliptical orbit in the inner solar system from its original orbit between Jupiter and Uranus (Królikowska and Szutowicz 2006). This comet was the target of NASA's highly successful STARDUST mission, which flew within 236 km of the nucleus to collect coma dust in January 2004 (Brownlee et al. 2003; 2004). Two years later, on January 15th, 2006, the STARDUST sample container returned safely to Earth, delivering the first *bona fide* cometary samples for laboratory analysis (Brownlee et al. 2006).

The STARDUST cometary sample collector employed two principal capture media: 1039 cm^2 of low-density silica aerogel in 132 individual cells and 153 cm^2 of 101 μm thick Al 1100 foil (> 99% Al) surrounding the aerogel cells (Tsou et al. 2003). The captured Wild 2 samples were first studied by a large and diverse international consortium during an initial six month period. This Preliminary Examination (PE) was organized into six topical teams, which recently reported their results with respect to organics (Sandford et al. 2006), bulk composition (Flynn et al. 2006), isotopes (McKeegan et al. 2006), optical properties (Keller et al. 2006), cratering and impact features (Hörz et al. 2006), as well as mineralogy-petrology (Zolensky et al. 2006). In this paper we report the detailed results of isotopic measurements of cometary debris in Al foil impact craters obtained with the NanoSIMS instruments at the Max Planck Institute for Chemistry in Mainz and at Washington University in St. Louis. Since both of these research groups were involved in the STARDUST PE, some of the results, most notably the discovery of the circumstellar grain, already found a brief mention in the isotope team overview paper (McKeegan et al. 2006).

The present analysis of actual Wild 2 cometary debris builds on an earlier feasibility study of impact features from laboratory test shots of Allende projectiles into STARDUST-type Al foils (Hoppe et al. 2006). There, we showed that it is possible to analyze hypervelocity impact residue at the bottom and on the rim of Al foil craters at high spatial resolution (better than 200 nm) with the NanoSIMS without requiring extensive sample preparation or modification for a

wide range of crater sizes (3 – 190 μm). We also demonstrated that it is possible to determine isotopic ratios of several light elements in such samples with a precision of several percent at a scale of several 100 nm, which is the typical size of presolar grains in primitive meteorites and IDPs. We concluded that we would be able to detect isotopically anomalous presolar matter in cometary dust residues in and around Al foil craters with this analytical approach, provided that such matter exists in the cometary samples and that it survives mechanical disruption, shock heating, and the intense mixing and homogenization of the resulting impact melts.

EXPERIMENTAL

The Al foil samples in this study were retrieved from the supporting frame of the STARDUST cometary sample collector using razor-sharp circular blades as illustrated in Figure SOM1 of Hörz et al. (2006). An overview of the samples analyzed here is given in Table 1. The sample names are comprised of the name of the cometary collector "C2", followed by the adjacent aerogel cell number (e.g., 086), followed by "W" for foils left ("West") or "N" for foils above ("North") of the respective aerogel tile (see http://curator.jsc.nasa.gov/stardust/sample_catalog for sample nomenclature). Since the majority of aerogel tiles are rectangular and oriented the same way, most "N" foil strips (including the ones in this study) are longer than "W" foil strips, 38 vs. 19 mm, respectively. The width of all foil strips is ~1.7 mm. After an initial optical characterization, some of the foil samples went through Time-of-flight Secondary Ion Mass Spectrometry (TOF-SIMS, Leitner et al. 2007) and/or Scanning Electron Microscopy – Energy Dispersive X-ray (SEM-EDX, Kearsley 2007) analyses, before being studied in the St. Louis or Mainz laboratories by SEM and NanoSIMS.

Table 1: Samples analyzed in this study

Foil Sample	Type	Size [μm]	Isotopes Measured	Laboratory
C2086N	large crater	59	C, N, O	Mainz
C2118N	large crater	72	C, N, O	St. Louis
C2013N	large crater	140	C, N, O	Mainz
C2086W	large penetration crater	~370	C, O	St. Louis
C2044W	10 small craters	0.32 – 1.2	O	Mainz
C2052N	31 small craters	0.51 – 1.5	O	Mainz
C2037N	6 small craters	0.61 – 1.9	C, N	Mainz

The measurements with the two CAMECA NanoSIMS instruments were done using slightly varying measurement conditions and different data processing routines, but in both cases followed the same underlying analytical approach (Hoppe et al. 2006). A 16 keV Cs^+ primary ion beam with a diameter of 50 – 100 nm and a current of ~1 pA was rastered over the sample surface for imaging in 128^2, 256^2, or 512^2 pixels. Up to five species of negative secondary ions and, in some cases, secondary electrons were simultaneously collected, and measurements were made in successive scans (layers) with total analysis times of up to several hours for areas ranging in size from 2 x 2 μm^2 to 30 x 30 μm^2. Images from different layers were added for each secondary ion species and the resulting isotope distribution images were processed following standard data routines for the identification of isotopic variations (e.g., Mostefaoui and Hoppe 2004; Stadermann et al. 2005a). We analyzed C, N, and O isotopes with the following secondary ion detector setups: [$^{12}C^-$, $^{13}C^-$, $^{16}O^-$, $^{17}O^-$, $^{18}O^-$] for C and O, [$^{16}O^-$, $^{17}O^-$, $^{18}O^-$, $^{28}Si^-$, $^{27}Al^{16}O^-$] for O, [$^{12}C^-$, $^{13}C^-$, $^{12}C^{14}N^-$, $^{12}C^{15}N^-$, $^{28}Si^-$] for C and N. All measurements were performed at sufficiently high mass resolution to avoid isobaric interferences. Note that N is measured as CN^- and that the $^{14}N/^{15}N$ isotopic ratio is determined from the $^{12}C^{14}N^-/^{12}C^{15}N^-$ ratio. Because of the

large morphological variations around the crater, it was not in all cases possible to use external standards for these measurements. This is due to the instrumental mass fractionation which can change by a few percent with sample height in the NanoSIMS. In such cases the results are relative to the 'bulk' of the material in the field of view of the crater measurements, which is assumed to be isotopically 'normal'. Consequently, such measurements are not suited to determine the bulk isotopic composition of the projectile debris. It is possible, however, to search for localized isotopic variations ("hotspots"), such as would be characteristic of presolar grains with extremely anomalous isotopic compositions

TOF-SIMS measurements were performed using a TOF-SIMS IV instrument from ION-TOF at the Institute for Planetology at Münster University (Stephan 2001). During the analyses, individual sample areas were rastered with a ~200 nm $^{69}Ga^{+}$ primary ion beam. Prior to the actual analyses, samples were sputter-cleaned by Ar^{+} ion bombardment. More details about analytical procedures are described by Leitner et al. (2007) where the results of all craters analyzed with TOF-SIMS during STARDUST PE are summarized.

Electron images and EDX maps of foils C2086N, C2086W, and C2118N were collected on a JEOL 5900LV SEM at the Natural History Museum (NHM) in London, fitted with an Oxford Instruments INCA X-sight EDX detector. All analyses were conducted with a 20 kV accelerating voltage and 2 nA beam current. Major and minor element quantitative EDX analyses employed the standard suite at the NHM (jadeite, Eagle Station pallasite olivine, synthetic corundum, wollastonite, Scandium phosphate, biotite, rutile and metallic V, Cr, Mn, and Ni). Foils were tilted to accommodate an appropriate extended Pouchou and Pichoir (XPP) matrix correction, following the protocols described in Kearsley et al. (2007). A detailed description of crater size, shape and residue composition for a wide range of other impact features can be found in Kearsley et al. (2007).

The crater residues on the foils C2013N, C2037N, C2044W, and C2052N were studied by SEM/EDX using a LEO 1530 Field Emission SEM equipped with an Oxford Instrument EDX system. Small (i.e. < 2 μm) craters were found by an automated survey of some 16 mm^2 surface area on the latter three foils with a lateral resolution of 100 nm. A total of 238 craters were found (Kearsley 2007), 47 of which were selected for NanoSIMS measurements. SEM/EDX data on the large craters in foils C2118N and C2086W were also acquired with a JEOL JSM-840A instrument with a Noran EDX detector.

RESULTS

Small craters

A total of 41 crater residues on Al foils C2044W (10 craters) and C2052N (31 craters) have been analyzed for O isotopic compositions. For 37 craters with sizes between 320 nm and 1.5 μm (median: 700 nm) we obtained useful isotopic data (three examples are shown in Fig. 1). In most cases we used the $^{28}Si^-$ image to determine the extent of the crater residue for calculating O isotopic ratios. Typical statistical errors for $^{17}O/^{16}O$ and $^{18}O/^{16}O$ ratios of individual crater residues are 5 – 6 % and 3 %, respectively. The O isotope data of all residues are compatible with solar and none of them exhibits a presolar signature (Fig. 2). Normalized to the O isotopic composition of contamination on the Al foil, we obtain average values of all crater residues of $\delta^{17}O = (-9 \pm 10)$ ‰ and $\delta^{18}O = (-10 \pm 5)$ ‰.

Additional systematic uncertainties of at least 1 – 2% (instrumental effects, absolute O isotopic composition of contamination on the Al foils, and matrix effects) should be considered for the SMOW-normalized O isotopic composition. Taking the empirical relationship crater size/impactor size = 4.6 (Kearsley et al. 2006) then the 37 crater residues studied here represent

some 0.14 μm^3 of cometary matter while a presolar silicate grain with a typical size of 300 nm has a volume of 0.014 μm^3.

Six craters from foil C2037N (610 nm – 1.9 μm, Fig. 3) were measured for C and N isotopic compositions by normalizing to measurements on nearby C- and N-rich contamination on the Al foil. The C isotopic ratios are close to normal with an average $\delta^{13}C$ of (-10 ± 7) ‰. Five crater residues have normal $^{15}N/^{14}N$ within 2σ, however one residue (crater #56), exhibits a small enrichment in ^{15}N with $\delta^{15}N$ of (+266 ± 65) ‰ (Fig. 4). The average $\delta^{15}N$ of the remaining small craters is (+104 ± 58) ‰.

In order to evaluate to what extent the C and N isotopic measurements are affected by crater topography, we also studied four craters (0.8 – 140 μm) which were produced in the laboratory by bombardment of a STARDUST-type Al foil with Admire pallasite olivine (the same projectiles described by Kearsley et al. 2007) at a velocity of ~6 km/s by use of the light gas gun facility at the University of Kent (Burchell et al. 1999). The impact craters were shown to contain some C and N, probably as a thin surface contamination layer derived from propellant residues as often occurs in light gas gun shots, although for the purpose of these test measurements, the precise origin is not important.

Three small craters (0.8, 3, and 4 μm) and two 10 x 10 μm^2 sized areas on the rim of one large crater (140 μm) were analyzed for C and N isotopic compositions. C and N isotopic ratios (Fig. 5) were normalized to those of surrounding contamination. On average, we obtained $\delta^{13}C$ = (-20 ± 2) ‰ with similar values for the small craters and the large crater. The non-zero value for $\delta^{13}C$ may reflect matrix effects (*i.e.*, difference in instrumental mass fractionation between the residue samples and the "standards") and/or true differences between the C isotopic compositions of the crater residues and the contamination on the Al foil. For $\delta^{15}N$ the numbers are slightly different for the small craters and the rim of the large crater. While the measurements

on the rim of the large crater yielded a $\delta^{15}N$ value compatible with zero, the measurements on the small craters give a weighted average $\delta^{15}N$ of (+54 ± 16) ‰. For O we observe only small differences (1-2 %) when the bulk O isotopic ratios of small and large laboratory-produced craters are compared (Hoppe et al. 2006). The test measurements reported here suggest that N measurements are possibly more sensitive to topographic effects than O (and C, see above) measurements. To account for this observation we have corrected the measured $^{15}N/^{14}N$ ratios of the small crater residues from foil C2037N for the average $\delta^{15}N$ measured on the laboratory-produced small craters, assuming that their true N isotopic compositions are normal as observed for the large crater.

Large crater in foil C2118N

This Al foil strip contains one large impact crater that was found during the routine optical scanning of the sample. We first performed an SEM-EDX analysis of this 72 μm diameter crater and then used the NanoSIMS to search for isotopic variations in projectile residue on the bottom and rim of the crater. The secondary electron images from the SEM and the NanoSIMS (Fig. 6) show the large crater in foil C2118N at high resolution. The coaxial beam optics of the NanoSIMS makes it possible to analyze material at the crater bottom and on the rim (Hoppe et al. 2006). These SE images appear to show relatively large chunks of debris throughout the crater. The differences between the SEM and the NanoSIMS secondary electron images are likely due to differences between ion- and electron-induced secondary electron emissions as well as extraction geometries.

We analyzed C, N, and O isotopes in this sample under standard conditions with the C-N and C-O detector setups (see Experimental). Because of the large size of this crater, it was not

possible to analyze the entire impact feature in a single NanoSIMS imaging measurement. Instead, the NanoSIMS measurements focused on areas on the crater rim that appeared to be residue-rich (Fig. 7) as well as on the crater bottom. Due to the large morphology variations around the crater and the resulting isotopic fractionations, external standards were not used for these measurements. The isotopic results for this crater are thus relative to 'bulk' of the material in the field of view. The locations of the NanoSIMS raster imaging measurements are shown in Fig. 8. Oxygen isotopes were not measured in area C, because sufficiently O-rich material could not be found following the C-N measurements.

Nitrogen isotopic imaging at the bottom of the crater revealed the presence of a grain whose N isotopic composition is enriched in ^{14}N. This C- and N-rich grain is indicated by the arrow in Figure 9. It has a $^{12}C/^{13}C$ ratio of 84 ± 5 (terrestrial = 89) and a $^{14}N/^{15}N$ ratio of 564 ± 97 (terrestrial = 272, *i.e.*, the anomaly is ~3 σ) which is similar to what is found in 'mainstream' presolar SiC grains (Zinner 2004). The anomalous grain originally had an approximate diameter of 150 nm. Unfortunately, the particle was sputtered away during the measurements, before further analyses could be made. Due to the relatively large uncertainty of this grain's isotopic composition and the fact that it was not possible to verify the anomaly in a follow-up measurement, we do not consider this grain to be of clear presolar origin. No other statistically significant isotopic variations of C, N, or O were observed in this impact crater.

Large craters in foils C2013N and C2086N

Residues in the large craters C2013N and C2086N were studied for C, N, and O isotopic compositions. Figure 10 shows SE images of both craters from the SEM-EDX characterization that preceded the NanoSIMS measurements. The chemical composition of the residue in both craters was determined by EDX, qualitatively for C2013N (scanning) and quantitatively for C2086N (scanning and spot analyses). C2086N was also analyzed by TOF-SIMS (Leitner et al.

2007). While the crater residue from foil C2013N exhibits a complex chemistry (with significant contributions from O, Na, Mg, Si, S, Fe), the residue from foil C2086N is probably derived from a single olivine grain of high forsterite content (Kearsley 2007; Leitner et al. 2007).

Table 2: Summary of O isotopic measurements on C2013N and C2086N residues.

Crater residue	Analyzed area [μm^2]	Recognized particles/subareas	Particle area [μm^2]	Average error $^{17}O/^{16}O$*	Average error $^{18}O/^{16}O$*
C2013N	5900	3640	1356	97 ‰	42 ‰
C2086N	3500	2409	955	97 ‰	41 ‰
Total	9400	6049	2311	97 ‰	42 ‰

* Per particle/subarea; based on counting statistics.

The results of the O isotopic measurements in theses craters are summarized in Table 2. The isotope measurements were made on material both from the crater rim and crater bottom. In total, one area with size 30 x 30 μm^2 (C2013N), as well as 50 (C2013N) and 35 (C2086N) areas with sizes of 10 x 10 μm^2 were investigated. These areas cover almost the whole crater in foil C2086N and most of the rim of crater C2013N. Automated particle recognition routines identified some 3600 (C2013N) and 2400 (C2086N) O-rich grains (or subareas) in the ion images. For all of these areas O isotopic ratios were calculated (normalized to the averages of $^{17}O/^{16}O$ and $^{18}O/^{16}O$ ratios in each area). The results are displayed in Fig. 11. One possible way to identify a particle as a presolar grain candidate is to see whether (a) $\delta^{17}O$ or $\delta^{18}O$ is > +200 ‰ or < -200 ‰ and (b) the anomaly is larger than 4σ, based on the counting statistical error plus systematic uncertainties due to crater topography which were estimated to be ~50 ‰ ($\delta^{17}O$) and ~20 ‰ ($\delta^{18}O$) for C2013N, as well as ~70 ‰ ($\delta^{17}O$) and ~35 ‰ ($\delta^{18}O$) for C2086N, respectively. A 3σ criterion is not sufficient because with the number of particles considered here several grains will fall outside this limit, simply for statistical reasons. The σ deviations for grains with

$\delta^{17}O > +200$ ‰ and < -200 ‰ are plotted in Fig. 12. There are a few grains outside 3σ, but no grain plots outside the 4σ limit. Given the O isotopic signatures of presolar silicates and the statistics of O isotopic ratios of the grains studied here, none of the particles from the craters C2013N and C2086N can unambiguously be identified as a circumstellar grain.

For the C and N isotopic measurements secondary ion images were acquired for 17 regions on the rim of crater C2013N, as well as nine regions on the rim and six regions on the bottom of crater C2086N, each 10 x 10 μm^2 in size. Thorough cleaning through sputtering prior to the isotope measurements was required to remove a C- and N-rich layer on the surface. C and N isotopic data were normalized to measurements on nearby C- and N-rich particulate contamination on the Al foil. In several areas we observed a strong $^{11}B^{16}O^-$ signal (possibly contamination from the glass container which was used for the foil shipment). The $^{11}B^{16}O^-$ peak can not be fully separated from the $^{12}C^{15}N^-$ peak even at the high mass resolving power used here. To avoid potential contributions from this interference to the $^{12}C^{15}N^-$ signal, the measurements in 11 regions on foil C2013N and in all regions on foil C2086N were performed on the low mass side of the center of the $^{12}C^{15}N^-$ peak. A test measurement on one of the surface contamination areas rich in C and N, where $^{11}B^{16}O^-$ was exceptionally high ($^{11}B^{16}O^-/^{13}C^{14}N^- \sim 9$, i.e. $^{11}B^{16}O^-/^{12}C^{15}N^- \sim 27$ for isotopically normal N), yielded a normal $^{15}N/^{14}N$ ratio, as expected.

Some 440 N-rich grains (or subareas) in crater C2013N, as well as 406 (rim) and 512 (bottom) subareas in crater C2086N were identified by an automated particle recognition routine. In general N concentrations are fairly low (at the permil level). The N from many of these grains/subareas of crater C2013N is isotopically heavy (Fig. 13). The average $\delta^{15}N$ of these N-rich particles/subareas is (+451 ± 7) ‰, the average $\delta^{13}C$ is (-25 ± 1) ‰. These errors are based on counting statistics alone. Additional systematic uncertainties of several percent in $\delta^{15}N$ and several permil in $\delta^{13}C$ should be considered for air and PDB normalized values, respectively. The entire analyzed crater C2013N has $\delta^{15}N$ = (+330 ± 4) ‰ and $\delta^{13}C$ = (-20 ± 1) ‰. In local

subareas $\delta^{15}N$ reaches +1000 ‰ or more (Fig. 13). This isotopic signature is similar to that observed in some isotopically primitive IDPs and in insoluble organic matter from carbonaceous chondrites (Floss et al. 2006; Busemann et al. 2006). It is possible that some C is still contamination since N is not well correlated with the overall distribution of C but seems to follow more closely the distribution of Si. In contrast, the C and N compositions of crater C2086N are isotopically normal on average (Fig. 13) with $\delta^{15}N = (-21 \pm 4)$ ‰ (rim) and (-1 ± 5) ‰ (bottom), respectively, and $\delta^{13}C = (-24 \pm 1)$ ‰ (rim) and (-18 ± 1) ‰ (bottom), respectively. Among the 918 N-rich grains/subareas in crater C2086N, there are only two objects which differ by ~ 4σ from normal N. We consider these to be outliers.

Large crater in foil C2086W

During extraction from the collector frame, this crater was identified as a complete penetration of the 101 μm thick Al foil, making it the largest impact feature yet studied on the foils. It now has an oval rim outline, with a maximum width of ~370 μm, although deformation during detachment from the underlying frame is probably responsible for this shape, caused by stretching of a circular feature that had an original diameter of ~240 μm. An initial optical evaluation of the detached foil (Fig. 14) indicated that a thin piece of Al foil was hanging from the back side of the penetration hole. This was probably part of the original crater bottom, torn free of the underlying frame to which it had become welded. Subsequent re-examination of the collector frame did not find any leftover debris or noticeable depression. The lack of an accessible bottom in this feature leaves the crater rim as the only area that is available for analysis.

Following the optical characterization, TOF-SIMS measurements showed clusters of material on the crater rim (Leitner et al. 2007) that are dominated by typical rock-forming elements, such as Si, Mg, Fe, Ca, reinforcing the identification of this material as residue from

the hypervelocity impact of cometary dust. TOF-SIMS elemental maps of the region that was subsequently investigated by NanoSIMS are shown in Figure 15. Figure 16 shows element ratios relative to Si and normalized to CI chondrites from an area selected from Fig. 15. Here most elements show abundances below chondritic values, which might be explained by a relative enrichment of Si in this fragment. Major rock-forming elements like Mg and Fe are depleted compared to Si, whereas C and Na are enriched. This might in part be due to contamination from the Al foil which is rather heterogeneous and therefore probably not accounted for completely in the blank correction of these data (Leitner et al. 2007), although high levels of Na associated with Ca were also found in silicate patches by use of EDX (see below). Figure 15 shows that S is also present in this area but it does not seem to be correlated with any major element, including Fe. Unfortunately, due to the lack of appropriate standards, the S abundance cannot be quantified in these measurements (Leitner et al. 2007).

After the TOF-SIMS measurement, this crater was analyzed by SEM-EDX. Abundant blocky residue was apparent on the crater walls, dominated by iron-rich silicate – probably olivine with a composition Forsterite (Fo) 65% Fayalite (Fa) 35% – associated with patches of Na and Ca-rich silicate which also contain P, S, K, Ti, and Mn above detection limits. A detailed description of the shape of this crater and EDX analyses of its residues are given in Kearsley et al. (2007). An overview image of the entire crater is shown in Figure 17, along with EDX maps showing the location of residue on the crater walls and rim.

A 20 x 20 μm^2 area on the rim of the crater was chosen for NanoSIMS C and O isotope imaging. This area included the large mass of projectile residue that is shown in the TOF-SIMS images in Fig. 15 and in the SEM image in Fig. 17. Although this material is located on the edge of the crater wall, it was possible to perform NanoSIMS imaging in this area. As discussed earlier, the extreme sample topography did not allow a determination of the absolute C and O isotopic compositions. However, it was possible to search for (relative) isotopic variations within

the images, on the assumption that the bulk of the material is isotopically normal within a few percent. The validity of this assumption is demonstrated by the fact that in all cases where absolute C and O isotopic measurements were possible (see above) the compositions were close to normal. These measurements led to the identification of a significantly ^{17}O-enriched hotspot with a diameter of ~250 nm as already summarized by McKeegan et al. (2006). The isotope imaging results are shown in Fig. 18, which consists of an overlay of a SE image and an isotope ratio image. Most of the analyzed area appears green in this figure portraying only minor local variations in the $^{17}O/^{16}O$ isotopic ratio. These variations are due to random statistical fluctuations as a result of the low overall O^- signal. The isotopically anomalous hotspot stands out from this material despite the fact that its anomalous composition is somewhat diluted as a result of the image 'smoothing' during the data processing. A detailed analysis of the imaging data indicates that the ^{17}O enrichment in this grain is more than +1500 ‰. This grain has a composition of $^{17}O/^{16}O = (1.01 \pm 0.10) \times 10^{-3}$ and $^{18}O/^{16}O = (1.77 \pm 0.12) \times 10^{-3}$, while normal isotopic ratios are 0.38×10^{-3} and 2.00×10^{-3}, respectively. Errors are 1 σ and are calculated from counting statistics. Repeated measurements of this area confirmed the presence of this ^{17}O-enriched hotspot.

Such an isotopic composition is typical for some types of circumstellar grains, as shown in the three-isotope-diagram (Fig. 19). It belongs to the 'group 1' O isotopic composition with a large ^{17}O enrichment and a slight ^{18}O depletion, which is indicative of an origin in red giant or asymptotic giant branch stars (Nittler et al. 1997). The three-isotope-diagram shows that although there may be differences in the statistical distribution of O isotopic anomalies between oxide and silicate grains, the most abundant type of anomaly in both cases are the ^{17}O-enriched 'group 1' compositions. The O isotopic composition of the circumstellar grain from comet Wild 2 falls close to the densest area of the diagram, representing the most typical compositions. The

C isotopic compositions of the hotspot and of all other areas of C2086W are normal within errors.

Unfortunately, there is no additional information about the elemental and mineralogical makeup of this presolar grain. A FIB extraction with subsequent TEM measurements (Chi 2007; Teslich 2007) did not lead to a successful identification of the grain, possibly because the presolar grain was already sputtered away during the NanoSIMS measurements. Based on the isotopic composition and the observed C and O secondary ion yields during the NanoSIMS measurements, it appears to be a silicate or oxide circumstellar grain. A distinction between these two types of presolar grains is not possible because no Si ion image was acquired.

DISCUSSION

Despite the fact that the STARDUST preliminary examination involved a large number of collaborating isotope groups (McKeegan et al. 2006) and extended to a variety of sample types beyond the Al foils discussed here, the sole circumstellar particle found so far is the one ^{17}O-rich grain in this study. On the one hand, this indicates that comet Wild 2 is not a pristine aggregate of presolar materials (McKeegan et al. 2006) and on the other hand it complements the observation that this comet contains high temperature components (e.g., Brownlee et al. 2006; Zolensky et al. 2006) that likely formed in the inner solar system (McKeegan et al. 2006). Both of these diverse components are found together in the cometary material, indicating that the comet Wild 2 preserved such heterogeneity largely unaltered in a 'cosmic freezer' for the last 4.5 billion years.

An essential question is the absolute abundance of circumstellar matter in the cometary samples. Such an abundance could then be compared with values for other types of

extraterrestrial matter such as primitive meteorites (Mostefaoui and Hoppe 2004; Nguyen et al. 2006), IDPs (Floss et al. 2006), and Antarctic micrometeorites (Yada et al. 2006). The concentration of circumstellar grains is frequently taken as a measure of the degree of 'primitiveness' of the parent body (Huss 1997). In this simplified model various extraterrestrial reservoirs are assumed to have started from similar original compositions in the early solar system with high concentrations of presolar components, which were subsequently modified to different degrees due to parent body processes, such as thermal metamorphism or aqueous alteration. Following this line of argument, Kuiper belt comets were thought to be prime candidates for high concentrations of presolar and circumstellar matter due to the excellent preservation conditions at the cold outer regions of the solar system (e.g., Hanner 2003).

The determination of an absolute abundance of circumstellar grains in samples from comet Wild 2 based on the available data is not a straightforward task. Complications arise from the poor statistics, with only one circumstellar grain being identified, from the varying analytical conditions and resulting detection efficiencies in different labs, from the mixing and interaction of the cometary matter with collector material in both aerogel and Al foils, and from unknown selection effects or survival probabilities during hypervelocity capture. Below we briefly discuss each of these factors.

Statistically speaking, one is a difficult number. This one circumstellar grain could have easily been missed if the residue-rich area on the rim of crater C2086W had not been measured for its O isotopic composition. The ensuing result of not finding any circumstellar grains in all of the analyzed Wild 2 samples would have dramatically altered our overall understanding of the comet. The Poisson uncertainty of a single observed event can be calculated as $1^{+4.68}_{-0.98}$ with 2σ errors (Gehrels 1986). Thus, the 2σ confidence interval extends from 0.02 to 5.68, representing an uncertainty of more than two orders of magnitude.

The next issues to address are the differences in analytical routines in different labs and the contrasting approaches to calculating abundances of circumstellar phases. This is not only due to instrumental differences but also a result of different mathematical models that are being used for data processing. Several recent studies reporting circumstellar grain abundances in various host phases (Messenger et al. 2003a; Floss et al. 2006; Nguyen et al. 2006; Vollmer et al. 2007) have used a variety of approaches that make it difficult to directly compare the results. Although each approach has its merits, the indiscriminate use of these divergent data processing routines artificially introduces an uncertainty as high as a factor of 2-3 even if only circumstellar grains > 200 nm are considered. The bottom line is that abundance comparisons are only valid within the context of a consistently applied mathematical model and constant analytical conditions.

Another difficult factor to evaluate results from the mixing and interaction of the cometary matter with the collector material in both aerogel and Al foils. Although this paper reports on Al foil impacts only, any calculation of circumstellar grain abundance has to take into account that none of the measurements on comet residues extracted from aerogel tracks has yielded a circumstellar grain to date. Fundamentally, the problem is that it is not always clear where the analyzed sample ends and the collection medium (or a contaminant) begins. This is particularly an issue in the aerogel samples, where aerogel is commonly rather intimately mixed with the sample on sub-micrometer scales (Zolensky et al. 2006; Stephan et al. 2007b). However, even on the Al foil residues the exact outline of the cometary matter is not always clear, as illustrated in the TOF-SIMS elemental maps. Since the circumstellar grain abundance is based on the ratio of two surface areas, one related to the isotopically anomalous material and the other to the isotopically "normal" reference area, an exact determination of the reference area is just as important as that of the isotopically anomalous region. We estimate the uncertainty resulting

from this difficulty to be on the order of a factor of 2 for Al foil samples and even higher for aerogel-extracted samples (Stephan et al. 2007a).

A final complicating factor is possible selection effects or varying survival probabilities during hypervelocity capture. The dust particles from comet Wild 2 collided with the collector at a relative velocity of 6.1 km/s. The resulting post-shock heating of the sample on the Al foil most likely led to melting of some of the impacting matter and some loss of volatile components. However, experimental studies of basalt glass, mafic silicate, and sulfide mineral grain impacts under these velocity conditions (Kearsley et al. 2007) have shown that it is likely that loss is restricted to S and a little Na, and other major and minor elements are retained at pre-impact levels in residue.

This discussion illustrates the complications with calculating an absolute circumstellar grain abundance in comet Wild 2 with the limited data available at this time. Overall, a relatively large number of samples have been analyzed for their isotopic compositions and the abundance of typical, isotopically highly anomalous grains is definitely not higher than what has been observed in IDPs and certain primitive meteorites, where values in the hundreds of ppm have been observed (Floss et al. 2006; Nguyen et al. 2006; Nagashima et al. 2004; Kobayashi et al. 2005; Vollmer et al. 2007). If we simply compare the area of the Wild 2 circumstellar grain with the estimated area of analyzed crater residue (~3000 μm^2) we obtain an abundance estimate of ~20 ppm, without making any corrections for detection efficiency. Given the aforementioned difficulties in calculating accurate circumstellar grain abundances, the true abundance could be significantly higher, yet taken at face value, the preliminary data obtained thus far suggest that the overall abundance of circumstellar grains is low compared to some other types of primitive solar system materials. If the abundance of circumstellar matter is an indicator of the primitiveness of a given parent body, this may suggest that comet Wild 2 is not more primitive – from an isotopic point of view – than other materials that have been studied in the past.

The observed isotopic characteristics of the analyzed cometary samples are, however, similar to what is seen elsewhere. We note a roughly normal isotopic composition of C, and we see 'bulk' type enrichments of ^{15}N as well as localized hotspots in some analyzed samples. This isotopic signature has been observed in a subgroup of IDPs termed "isotopically primitive" (Floss et al. 2006). Among IDPs, circumstellar grains appear exclusively in this subgroup of IDPs (Floss et al. 2006) and thus the similar N isotopic compositions are also consistent with finding a circumstellar grain in the cometary matter. This observation could hint at a genetic relationship between IDPs and comets, as has been often suggested in the past (e.g., Messenger et al. 2003a). However, we note that carbonaceous matter from some primitive meteorites exhibits N isotopic distributions similar to those seen in IDPs (Floss and Stadermann 2005; Busemann et al. 2006), suggesting that it may be a more fundamental property of all primitive solar system matter. The present study did not find any components in the cometary dust similar to the extremely ^{13}C-poor particle observed during a flyby at comet Halley (Jessberger and Kissel 1991).

Another interesting question is how the bulk O isotopic composition of Wild 2 matter compares with that of chondrites. The average O isotopic composition of the residues in the small craters falls at the low end of what is observed for $\delta^{17}O$ and $\delta^{18}O$ in carbonaceous chondrites, overlapping with the composition of CO/CV chondrites (Clayton 1993). However, if we consider the systematic uncertainties of at least 1-2 % in addition to the errors given above for small craters, then the O isotope data for the crater residues are also compatible with the bulk composition of CM and CI chondrites. Thus, based on the O isotopic signature of the small crater residues, it is not possible to establish a clear relationship to one of the carbonaceous chondrite groups.

This study is clearly only the beginning of many detailed characterizations of the cometary material returned by the STARDUST spacecraft. Once a statistically more solid

database of circumstellar grains and other isotopic effects in these samples has been acquired, it will be possible to better evaluate the rank of Wild 2 cometary matter among the most primitive solar system materials available for laboratory research. The next step from there will be an evaluation of how representative the material from comet Wild 2 might be for Kuiper Belt comets in general. Since only a small fraction of the returned samples has been investigated during the preliminary examination and analytical techniques are increasingly being optimized for ever smaller samples, the Wild 2 cometary samples will be the objects of interest for many years to come.

Acknowledgements: The St. Louis portion of this work was supported by NASA grant NNG05GJ26G. TOF-SIMS measurements in Münster were supported by the Deutsche Forschungsgemeinschaft through grant STE 576/17-1. We thank Elmar Gröner and Tim Smolar for technical assistance with the NanoSIMS instruments in Mainz and St. Louis, respectively.

REFERENCES

[Note to the reviewers: There are several incomplete references below. They all are cross-references to other articles that are expected to appear in the same special issue of MAPS. Since titles, author lists and even acceptance can still change for those papers, these references will have to remain in this provisional form until after the review.]

Boss A. P. 2004. Evolution of the solar nebula. VI. Mixing and transport of isotopic heterogeneity. *Astrophys. J.* 616:1265-1277.

Brownlee D., Tsou P., Aléon J., Alexander C. M. O. D., Araki T., Bajt S., Baratta G. A., Bastien R., Bland P., Bleuet P., Bort J., Bradley J. P., Brearley A., Brenker F., Brennan S., Bridges J. C., Browning N. D., Brucato J. R., Brucato H., Bullock E., Burchell M. J., Busemann H., Butterworth A., Chaussidon M., Cheuvront A., Chi M., Cintala M. J., Clark B. C., Clemett S. J., Cody G., Colangeli L., Cooper G., Cordier P., Daghlian C., Dai Z., D'Hendecourt L., Djouadi Z., Dominguez G., Duxbury T., Dworkin J. P., Ebel D. S., Economou T. E., Fakra S., Fairey S. A. J., Fallon S., Ferrini G., Ferroir T., Fleckenstein H., Floss C., Flynn G., Franchi I. A., Fries M., Gainsforth Z., Gallien J.-P., Genge M., Gilles M. K., Gillet P., Gilmour J., Glavin D. P., Gounelle M., Grady M. M., Graham G. A., Grant P. G., Green S. F., Grossemy F., Grossman L., Grossman J. N., Guan Y., Hagiya K., Harvey R., Heck P., Herzog G. F., Hoppe P., Hörz F., Huth J., Hutcheon I. D., Ignatyev K., Ishii H., Ito M., Jacob D., Jacobsen C., Jacobsen S., Jones S., Joswiak D., Jurewicz A., Kearsley A. T., Keller L. P., Khodja J., Kilcoyne A. L. D., Kissel J., Krot A., Langenhorst F., Lanzirotti A., Le L., Leshin L. A., Leitner J., Lemelle L., Leroux H., Liu M.-C., Luening K., et al. 2006. Comet 81P/Wild 2 under a microscope. *Science* 314:1711-1716.

Brownlee D. E., Tsou P., Anderson J. D., Hanner M. S., Newburn R. L., Sekanina Z., Clark B. C., Hörz F., Zolensky M. E., Kissel J., McDonnell J. A. M., Sandford S. A., and Tuzzolino A. J. 2003. Stardust: Comet and interstellar dust sample return mission. *J. Geophys. Res.* 108:1-15.

Brownlee D. E., Hörz F., Newburn R. L., Zolensky M., Duxbury T. C., Sandford S., Sekanina Z., Tsou P., Hanner M. S., Clark B. C., Green S. F., and Kissel J. 2004. Surface of young Jupiter family comet 81P/Wild 2: View from the Stardust spacecraft. *Science* 304:1764-1769.

Burchell M. J., Cole M. J., McDonnell J. A. M., and Zarnecki J. C. 1999. Hypervelocity impact studies using the 2 MV Van de Graaff dust accelerator and two stage Light Gas Gun of the University of Kent at Canterbury. *Measurement Science and Technology* 10:41-50.

Busemann H., Young A. F., Alexander C. M. O. D., Hoppe P., Mukhopadhyay S., and Nittler L. R. 2006. Interstellar chemistry recorded in organic matter from primitive meteorites. *Science* 312:727-730.

Chi. 2007. --to be added---. *this volume*.

Clayton R. N. 1993. Oxygen isotopes in meteorites. In *Ann. Rev. Earth Planet. Sci.*, Vol. 21 edited by G. W. Wetherill, A. L. Albee, and K. C. Burke, pp. 115-149.

Floss C., Stadermann F. J., Bradley J., Dai Z. R., Bajt S., and Graham G. 2004. Carbon and nitrogen isotopic anomalies in an anhydrous interplanetary dust particle. *Science* 303:1355-1358.

Floss C. and Stadermann F. J. 2005. Presolar (circumstellar and interstellar) phases in Renazzo: The effects of parent body processing. *Lunar Planet. Sci.* XXXVI:Abstract #1390.

Floss C., Stadermann F. J., Bradley J. P., Dai Z. R., Bajt S., Graham G., and Lea A. S. 2006. Identification of isotopically primitive interplanetary dust particles: A NanoSIMS isotopic imaging study. *Geochim. Cosmochim. Acta* 70:2371-2399.

Flynn G. J., Bleuet P., Borg J., Bradley J. P., Brenker F. E., Brennan S., Bridges J., Brownlee D. E., Bullock E. S., Burghammer M., Clark B. C., Dai Z. R., Daghlian C. P., Djouadi Z., Fakra S., Ferroir T., Floss C., Franchi I. A., Gainsforth Z., Gallien J.-P., Gillet P., Grant P. G., Graham G. A., Green S. F., Grossemy F., Heck P., Herzog G. F., Hoppe P., Hörz F., Huth J., Ignatyev K., Ishii H. A., Janssens K., Joswiak D., Kearsley A. T., Khodja H., Lanzirotti A., Leitner J., Lemelle L., Leroux H., Luening K., MacPherson G. J., Marhas K. K., Marcus M. A., Matrajt G., Nakamura T., Nakamura-Messenger K., Nakano T., Newville M., Papanastassiou D. A., Pianetta P., Rao W., Riekel C., Rietmeijer F. J. M., Rost D., Schwandt C. S., See T. H., Sheffield-Parker J., Simionovici A., Sitnitsky I., Snead C. J., Stadermann F. J., Stephan T., Stroud R. M., Susini J., Suzuki Y., Sutton S. R., Taylor S., Teslich N., Troadec D., Tsou P., Tsuchiyama A., Uesugi K., Vekemans B., Vicenzi E. P., Vincze L., Westphal A. J., Wozniakiewicz P., Zinner E., and Zolensky M. E. 2006. Elemental compositions of comet 81P/Wild 2 samples collected by Stardust. *Science* 314:1731-1735.

Gehrels N. 1986. Confidence limits for small numbers of events in astrophysical data. *Astrophys. J.* 303:336-346.

Hanner M. S. 2003. The Mineralogy of Cometary Dust. In *Astromineralogy* edited by T. Henning, pp. 171-188. Springer.

Hoppe P., Mostefaoui S., and Stephan T. 2005. NanoSIMS oxygen and sulfur-isotope imaging of primitive Solar System materials. *Lunar Planet. Sci.* XXXVI:Abstract #1301.

Hoppe P., Stadermann F. J., Stephan T., Floss C., Leitner J., Marhas K. K., and Hörz F. 2006. SIMS studies of Allende projectiles fired into Stardust-type aluminum foils at 6 km/sec. *Meteorit. Planet. Sci.* 41:197-209.

Hörz F., Bastien R., Borg J., Bradley J. P., Bridges J. C., Brownlee D. E., Burchell M. J., Chi M., Cintala M. J., Dai Z. R., Djouadi Z., Dominguez G., Economou T. E., Fairey S. A. J., Floss C., Franchi I. A., Graham G. A., Green S. F., Heck P., Hoppe P., Huth J., Ishii H., Kearsley A. T., Kissel J., Leitner J., Leroux H., Marhas K., Messenger K., Schwandt C. S., See T. H., Snead C., Stadermann F. J., Stephan T., Stroud R., Teslich N., Trigo-Rodríguez J. M., Tuzzolino A. J., Troadec D., Tsou P., Warren J., Westphal A., Wozniakiewicz P., Wright I., and Zinner E. 2006. Impact features on Stardust: Implications for comet 81P/Wild 2 dust. *Science* 314:1716-1719.

Huss G. R. 1997. The survival of presolar grains in solar system bodies. In *Astrophysical Implications of the Laboratory Study of Presolar Materials* edited by T. J. Bernatowicz and E. Zinner, pp. 721-748. AIP.

Jessberger E. K. and Kissel J. 1991. Chemical properties of cometary dust and a note on carbon isotopes. In *Comets in the Post-Halley Era* edited by R. N. e. al., pp. 1075-1092. Springer Verlag.

Kearsley A. T., Burchell M. J., Hörz F., Cole M. J., and Schwandt C. S. 2006. Laboratory simulation of impacts on aluminum foils of the Stardust spacecraft: Calibration of dust particle size from comet Wild-2. *Meteorit. Planet. Sci.* 41:167-180.

Kearsley A. T. 2007. --to be added--. *this volume*.

Kearsley A. T., Graham G. A., Burchell M. J., Cole M. J., Dai Z. R., Teslich N., Bradley J. P., Chater R., Wozniakiewicz P. A., Spratt J., and Jones G. 2007. Analytical scanning and transmission electron microscopy of laboratory impacts on Stardust aluminum foils: interpreting impact crater morphology and the composition of impact residues. *Meteorit. Planet. Sci.* 42:in press.

Keller L. P., Bajt S., Baratta G. A., Borg J., Bradley J. P., Brownlee D. E., Busemann H., Brucato J. R., Burchell M., Colangeli L., d'Hendecourt L., Djouadi Z., Ferrini G., Flynn G., Franchi I. A., Fries M., Grady M. M., Graham G. A., Grossemy F., Kearsley A., Matrajt G., Nakamura-Messenger K., Mennella V., Nittler L., Palumbo M. E., Stadermann F. J., Tsou P., Rotundi A., Sandford S. A., Snead C., Steele A., Wooden D., and Zolensky M. 2006. Infrared spectroscopy of comet 81P/Wild 2 samples returned by Stardust. *Science* 314:1728-1731.

Kobayashi S., Tonotani A., Sakamoto N., Nagashima K., Krot A. N., and Yurimoto H. 2005. Abundances of presolar silicates in primitive carbonaceous chondrites Yamato-81025, ALHA 77307, Adelaide and Acfer 094. *Antarctic Meteorites* XXIX:30-31.

Królikowska M. and Szutowicz S. 2006. Non-gravitational motion of the Jupiter-family comet 81P/Wild 2. *Astron. & Astrophys.* 448:401-409.

Leitner J., Stephan T., Kearsley A. T., Hörz F., Flynn G. J., and Sandford S. A. 2007. TOF-SIMS analysis of crater residues from Wild 2 cometary particles on Stardust aluminum foil. *Meteorit. Planet. Sci.*:submitted.

Levison H. F. and Duncan M. J. 1997. From the Kuiper belt to Jupiter-family comets: The spatial distribution of ecliptic comets. *Icarus* 127:13-32.

McKeegan K. D., Aléon J., Bradley J., Brownlee D., Busemann H., Butterworth A., Chaussidon M., Fallon S., Floss C., Gilmour J., Gounelle M., Graham G., Guan Y., Heck P. R., Hoppe P., Hutcheon I. D., Huth J., Ishii H., Ito M., Jacobsen S. B., Kearsley A., Leshin L. A., Liu M.-C., Lyon I., Marhas K., Marty B., Matrajt G., Meibom A., Messenger S., Mostefaoui S., Mukhopadhyay S., Nakamura-Messenger K., Nittler L., Palma R., Pepin R. O., Papanastassiou D. A., Robert F., Schlutter D., Snead C. J., Stadermann F. J., Stroud R., Tsou P., Westphal A., Young E. D., Ziegler K., Zimmermann L., and Zinner E. 2006. Isotopic compositions of cometary matter returned by Stardust. *Science* 314:1724-1728.

Messenger S., Keller L. P., Stadermann F. J., Walker R. M., and Zinner E. 2003a. Samples of stars beyond the solar system: Silicate grains in interplanetary dust. *Science* 300:105-108.

Messenger S., Stadermann F. J., Floss C., Nittler L. R., and Mukhopadhyay S. 2003b. Isotopic signatures of presolar materials in interplanetary dust. *Space Sci. Rev.* 106:155-172.

Messenger S., Keller L. P., and Lauretta D. S. 2005. Supernova olivine from cometary dust. *Science* 309:737-741.

Mostefaoui S. and Hoppe P. 2004. Discovery of abundant in situ silicate and spinel grains from red giant stars in a primitive meteorite. *Astrophys. J.* 613:L149-L152.

Nagashima K., Krot A. N., and Yurimoto H. 2004. Stardust silicates from primitive meteorites. *Nature* 428:921-924.

Nguyen A. N. and Zinner E. 2004. Discovery of ancient silicate stardust in a meteorite. *Science* 303:1496-1499.

Nguyen A. N., Zinner E., and Stroud R. M. 2005. Continued characterization of presolar silicate grains from the Acfer 094 carbonaceous chondrite. *Lunar Planet. Sci.* XXXVI:Abstract #2196.

Nguyen A. N., Stadermann F. J., Zinner E., Stroud R. M., Alexander C. M. O. D., and Nittler L. R. 2006. Characterization of presolar silicate and oxide grains in primitive carbonaceous chondrites. *Astrophys. J.*:submitted.

Nittler L. R., Alexander C. M. O. D., Gao X., Walker R. M., and Zinner E. K. 1994. Interstellar oxide grains from the Tieschitz ordinary chondrite. *Nature* 370:443-446.

Nittler L. R., Alexander C. M. O. D., Gao X., Walker R. M., and Zinner E. 1997. Stellar sapphires: The properties and origins of presolar Al_2O_3 in meteorites. *Astrophys. J.* 483:475-495.

Nittler L. R., Alexander C. M. O. D., Wang J., and Gao X. 1998. Meteoritic oxide grain from supernova found. *Nature* 393:222.

Sandford S. A., Aléon J., Alexander C. M. O. D., Araki T., Bajt S., Baratta G. A., Borg J., Bradley J. P., Brownlee D. E., Brucato J. R., Burchell M. J., Busemann H., Butterworth A., Clemett S. J., Cody G., Colangeli L., Cooper G., D'Hendecourt L., Djouadi Z., Dworkin J. P., Ferrini G., Fleckenstein H., Flynn G. J., Franchi I. A., Fries M., Gilles M. K., Glavin D. P., Gounelle M., Grossemy F., Jacobsen C., Keller L. P., Kilcoyne A. L. D., Leitner J., Matrajt G., Meibom A., Mennella V., Mostefaoui S., Nittler L. R., Palumbo M. E., Papanastassiou D. A., Robert F., Rotundi A., Snead C. J., Spencer M. K., Stadermann F. J., Steele A., Stephan T., Tsou P., Tyliszczak T., Westphal A. J., Wirick S., Wopenka B., Yabuta H., Zare R. N., and Zolensky M. E. 2006. Organics captured from comet 81P/Wild 2 by the Stardust spacecraft. *Science* 314:1720-1724.

Scott E. R. D. and Krot A. N. 2005. Chondritic meteorites and the high-temperature nebular origins of their components. In *Chondrites and the Protoplanetary Disk, ASP Conf. Series*, Vol. 341 edited by A. N. Krot, E. R. D. Scott, and B. Reipurth, pp. 15-53. Astronomical Soc. of the Pacific.

Stadermann F. J., Croat T. K., Bernatowicz T. J., Amari S., Messenger S., Walker R. M., and Zinner E. 2005a. Supernova graphite in the NanoSIMS: Carbon, oxygen and titanium isotopic compositions of a spherule and its TiC sub-components. *Geochim. Cosmochim. Acta* 69:177-188.

Stadermann F. J., Floss C., Bland P. A., Vicenzi E. P., and Rost D. 2005b. An oxygen-18 rich presolar silicate grain from the Acfer 094 meteorite: A NanoSIMS and TOF-SIMS study. *Lunar Planet. Sci.* XXXVI:Abstract #2004.

Stephan T. 2001. TOF-SIMS in cosmochemistry. *Planet. & Space Sci.* 49:859-906.

Stephan T., Flynn G. J., Sandford S. A., and Zolensky M. E. 2007a. TOF-SIMS analysis of cometary particles extracted from Stardust aerogel. *Meteorites and Planetary Science*(this issue).

Stephan T., Rost D., Vicenzi E. P., Bullock E. S., MacPherson G. J., Westphal A. J., Snead C. J., Flynn G. J., Sandford S. A., and Zolensky M. E. 2007b. TOF-SIMS analysis of cometary matter in Stardust aerogel tracks. *Meteorites and Planetary Science*(this issue).

Teslich. 2007. --to be added--. *this volume.*

Tsou P., Brownlee D. E., Sandford S. A., Hörz F., and Zolensky M. E. 2003. Wild 2 and interstallar sample collection and Earth return. *J. Geophys. Res.* 108:(E10), 8113.

Vollmer C., Hoppe P., Brenker F., and Holzapfel C. 2007. A presolar silicate trilogy: Condensation, coagulation and transformation: New insights from NanoSIMS-TEM investigations. *Lunar Planet. Sci.*:submitted.

Yada T., Stadermann F. J., Floss C., Zinner E., Nakamura T., Noguchi T., and Lea A. S. 2006. High abundances of presolar silicates in Antarctic micrometeorites; implications for their cometary origins. *Lunar Planet. Sci.* XXXVII:Abstract #1470.

Zinner E. 1988. Interstellar cloud material in meteorites. In *Meteorites and the Early Solar System* edited by J. F. Kerridge and M. S. Matthews, pp. 956-983. University of Arizona Press.

Zinner E. 2004. Presolar grains. In *Meteorites, Planets, and Comets (Ed. A. M. Davis), Vol. 1 Treatise on Geochemistry (Eds. H. D. Holland and K. K. Turekian)*, Vol. 1 edited, pp. 17-39. Elsevier-Pergamon, Oxford.

Zinner E., Nittler L. R., Hoppe P., Gallino R., Straniero O., and Alexander C. M. O. D. 2005. Oxygen, magnesium and chromium isotopic ratios of presolar spinel grains. *Geochim. Cosmochim. Acta* 69:4149-4165.

Zolensky M. E., Zega T. J., Yano H., Wirick S., Westphal A. J., Weisberg M. K., Weber I., Warren J. L., Velbel M. A., Tsuchiyama A., Tsou P., Toppani A., Tomioka N., Tomeoka K., Teslich N., Taheri M., Susini J., Stroud R., Stephan T., Stadermann F. J., Snead C. J., Simon S. B., Simionovici A., See T. H., Robert F., Rietmeijer F. J. M., Rao W., Perronnet M. C., Papanastassiou D. A., Okudaira K., Ohsumi K., Oshnishi I., Nakamura-Messenger K., Nakamura T., Mostefaoui S., Mikouchi T., Meibom A., Matrajt G., Marcus M. A., Leroux H., Lemelle L., Le L., Lanzirotti A., Langenhorst F., Krot A. N., Keller L. P., Kearsley A. T., Joswiak D., Jacob D., Ishii H., Harvey R., Hagiya K., Grossman L., Grossman J. N., Graham G. A., Gounelle M., Gillet P., Genge M. J., Flynn G., Ferroir T., Fallon S., Ebel D. S., Dai Z. R., Cordier P., Clark B., Chi M., Butterworth A. L., Brownlee D. E., Bridges J. C., Brennan S., Brearley A., Bradley J. P., Bleuet P., Bland P. A., and Bastien R. 2006. Mineralogy and petrology of comet 81P/Wild 2 nucleus samples. *Science* 314:1735-1739.

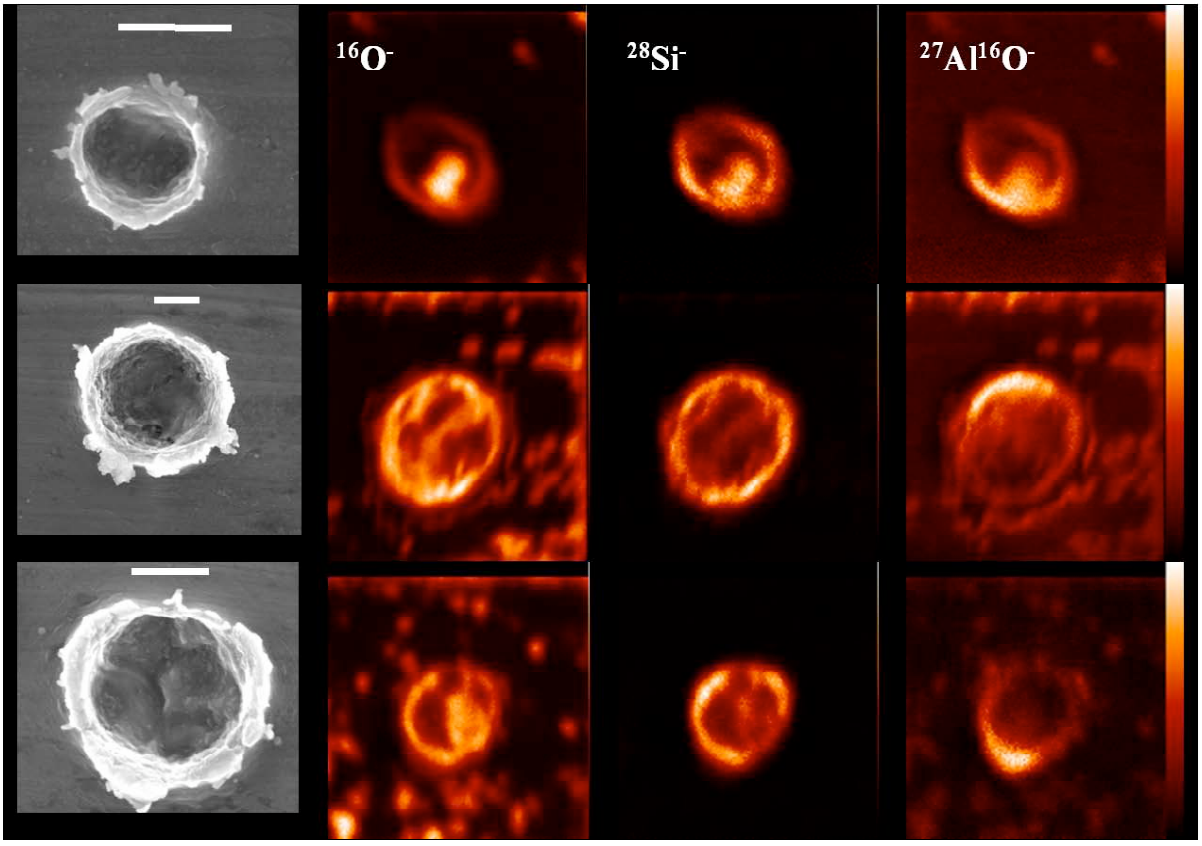

Figure 1: SEM and NanoSIMS ion images of $^{16}O^-$, $^{28}Si^-$, and $^{27}Al^{16}O^-$ of selected craters on foil C2052N (top: #40, middle: #82, bottom: #126). The ion images are false-color images where the minimum intensity in each image is shown in black and the maximum intensity in white (see color bars on right). Scale bars in SEM images: 500 nm. Field of view in the ion images: 3 x 3 μm^2.

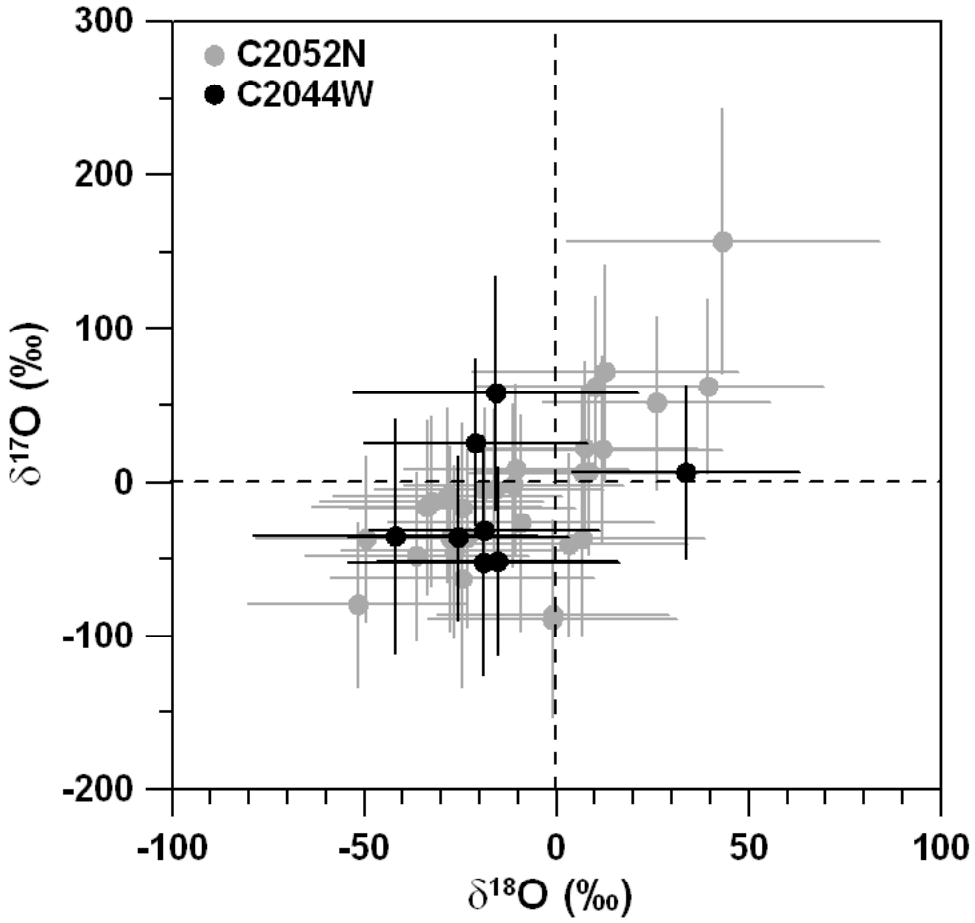

Figure 2: O isotopic compositions (normalized to nearby contamination) of 37 crater residues from two Stardust Al foils (C2044W, C2052N). Errors are 1σ and include the counting statistical errors as well as the spot-to-spot reproducibility of O isotopic ratio measurements on the nearby contamination.

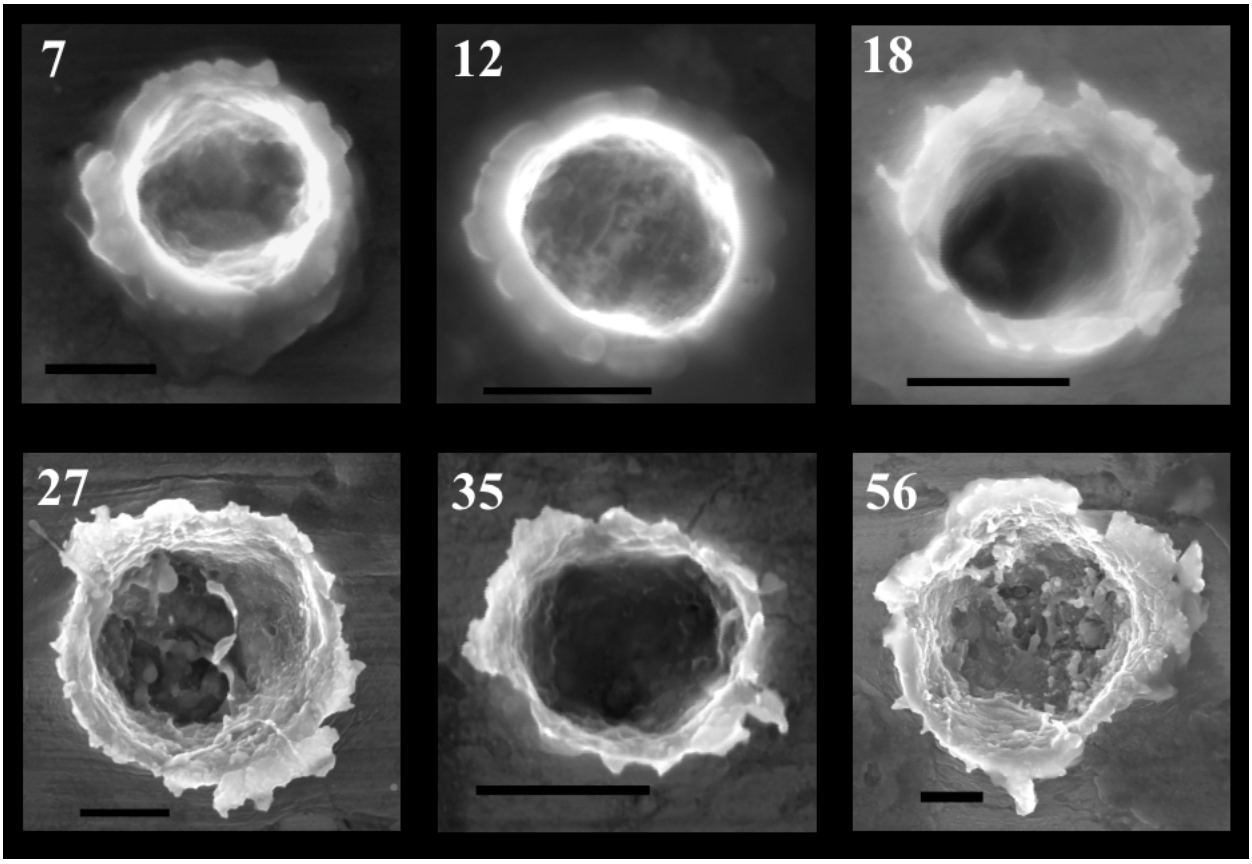

Figure 3: SEM images of small craters in Al foil C2037N. Scale bars are 500 nm and the numbers refer to crater identification.

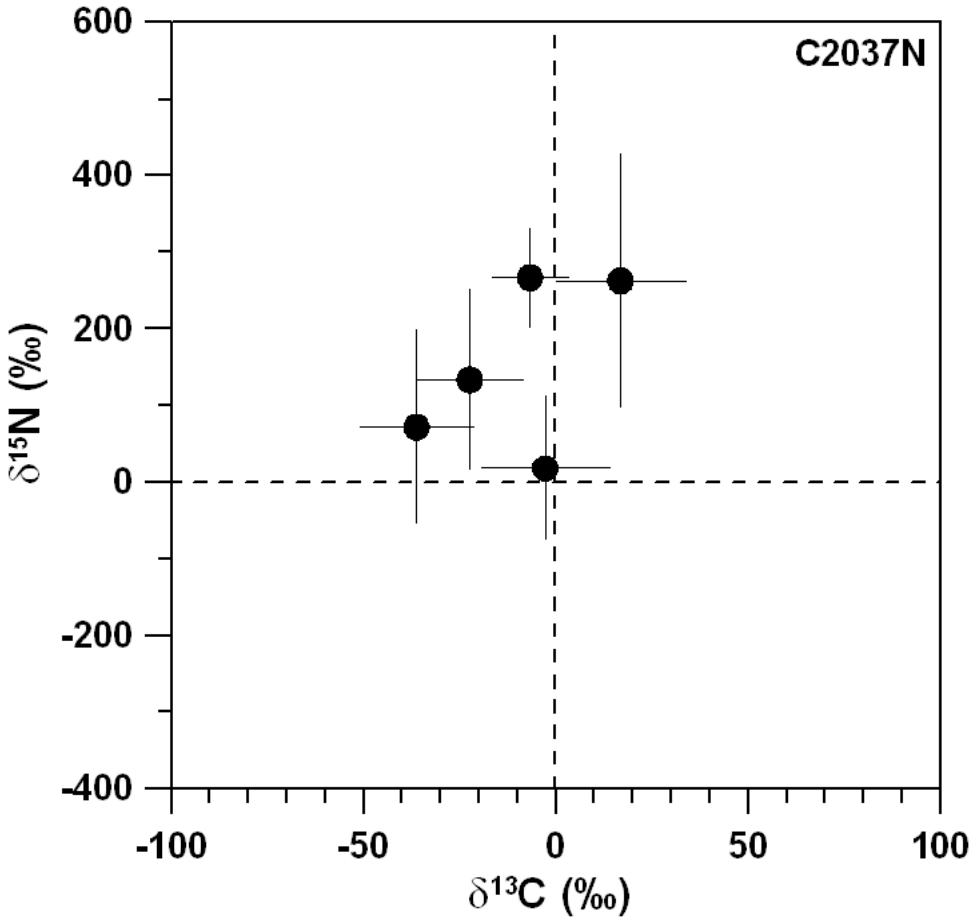

Figure 4: C and N isotopic compositions of crater residues on Al foil C2037N (normalized to contamination on the foil). Errors are 1σ and include the counting statistical errors as well as the spot-to-spot variability of C and N isotopic ratio measurements on the nearby contamination. Data are shown for those residues that have an uncertainty of less than 200 ‰ in $\delta^{15}N$.

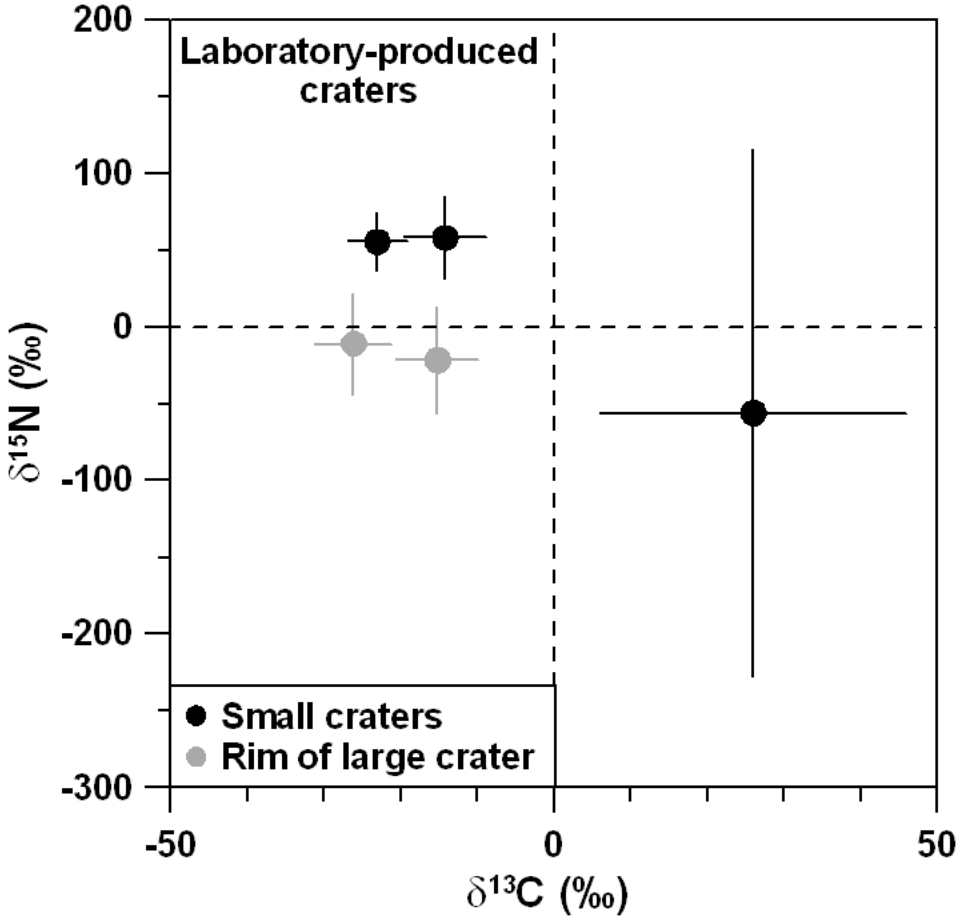

Figure 5: C and N isotopic compositions of Admire olivine crater residues from laboratory produced craters (normalized to contamination on the foil). Errors are 1σ and are based on counting statistics.

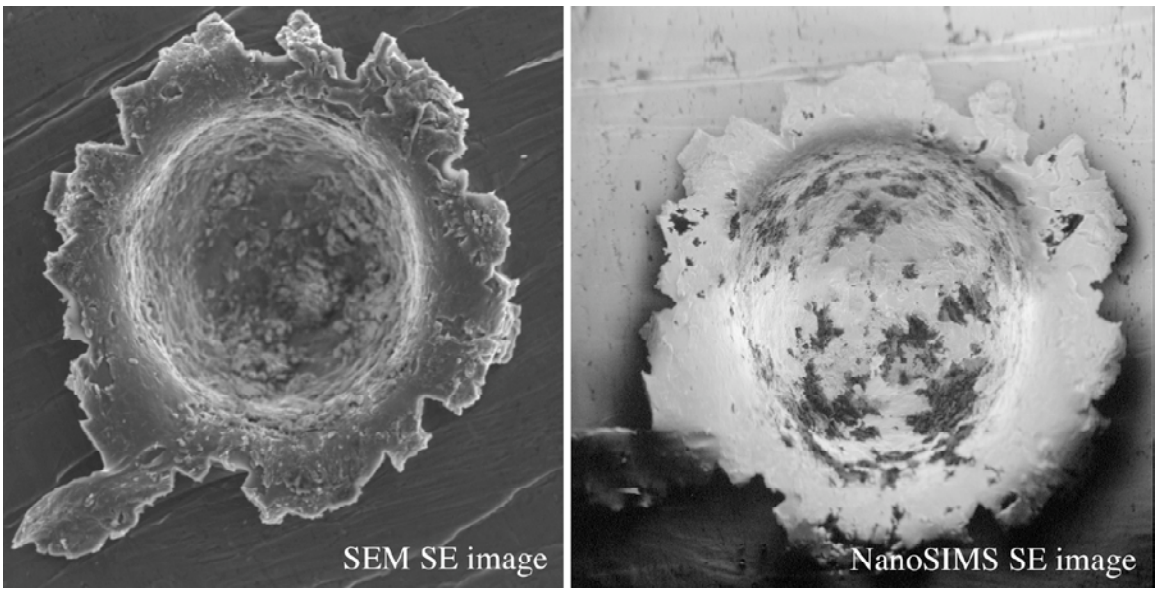

Figure 6: Secondary electron images of crater C2118N taken with the SEM and with the NanoSIMS. The diameter of this crater is 72 µm.

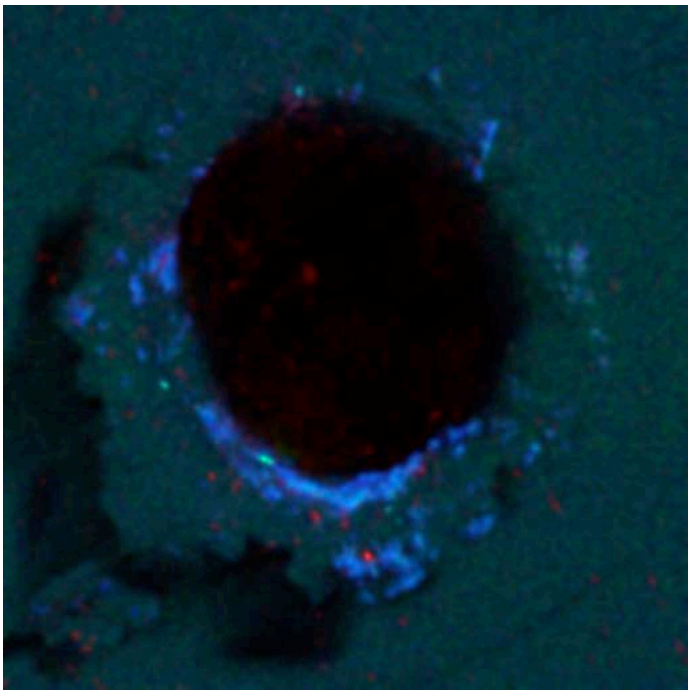

Figure 7: X-ray RGB map of crater C2118N obtained during SEM-EDX characterization. In this false color image, brighter colors represent higher abundances of Fe (red), Mg (green) and Si (blue). Areas of projectile residue with Si-rich material as well as some Fe and Mg hotspots are visible along the crater rim. Note that the crater bottom appears dark due to shading as a result of the detector geometry in the SEM.

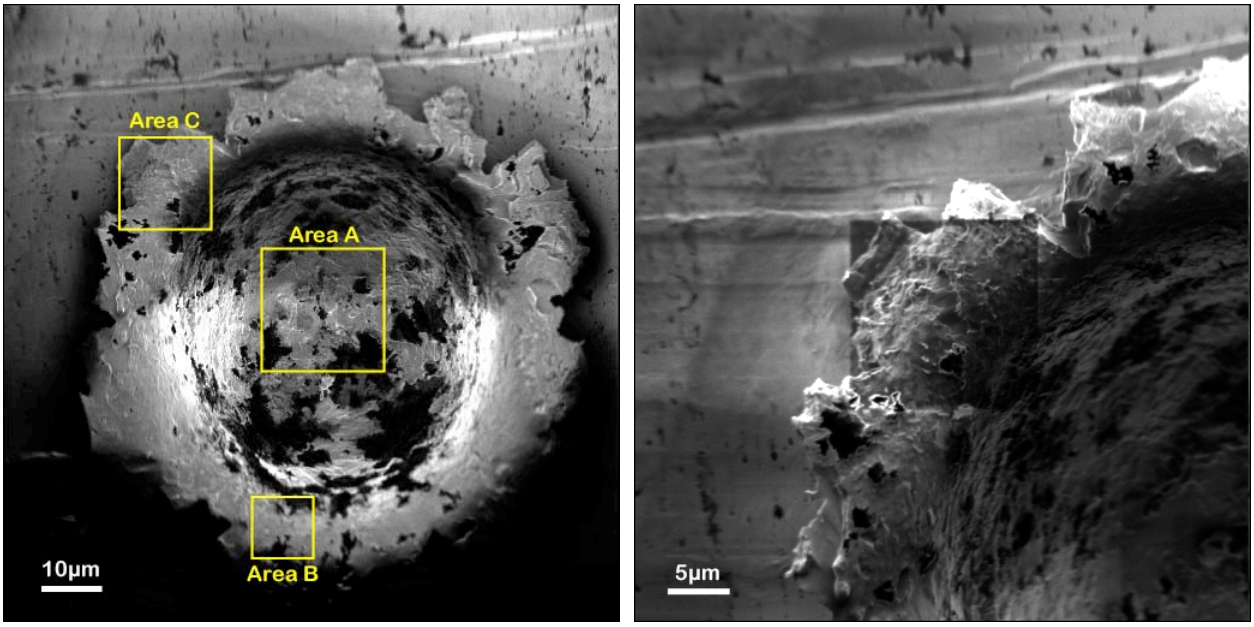

Figure 8: Location of NanoSIMS measurements in crater C2118N (left). Measurements were made in areas A (20 x 20 µm^2), B (10 x 10 µm^2), and C (15 x 15 µm^2). The sputtered area C is clearly visible on the crater rim after the measurement (right).

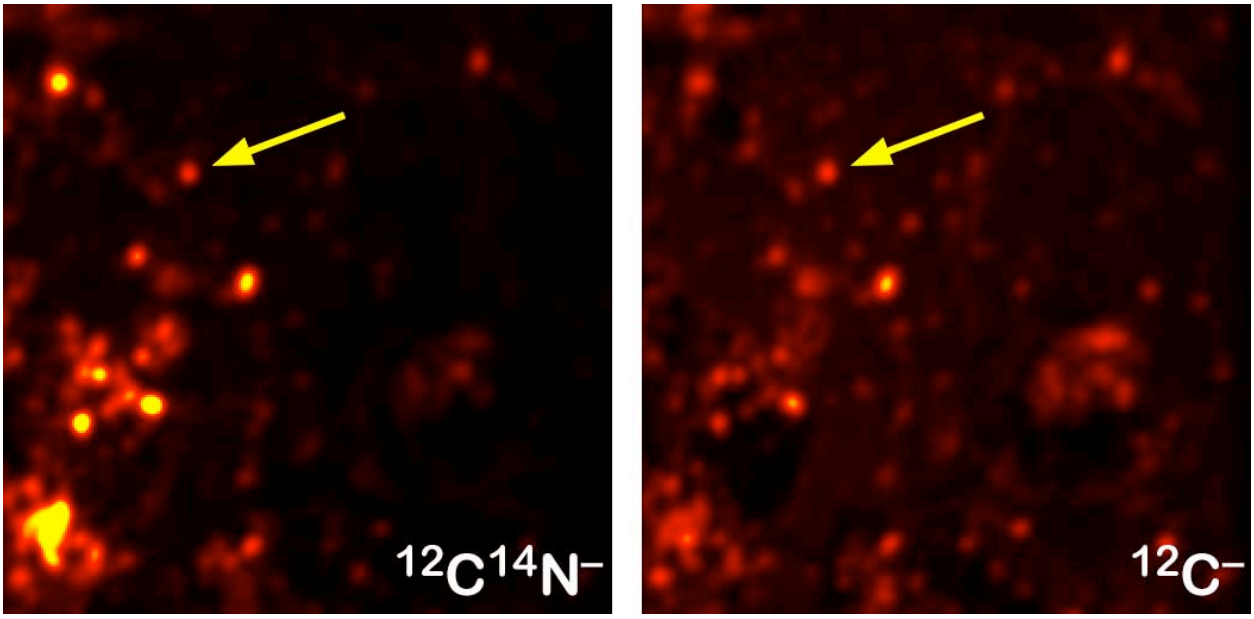

Figure 9: Elemental distribution images of a 10 x 10 µm² region (a subarea of 'A', Fig. 8) at the bottom of crater C2118N. The C- and N-rich grain indicated by the arrow has an anomalous N isotopic composition, but was sputtered away rapidly during the measurement.

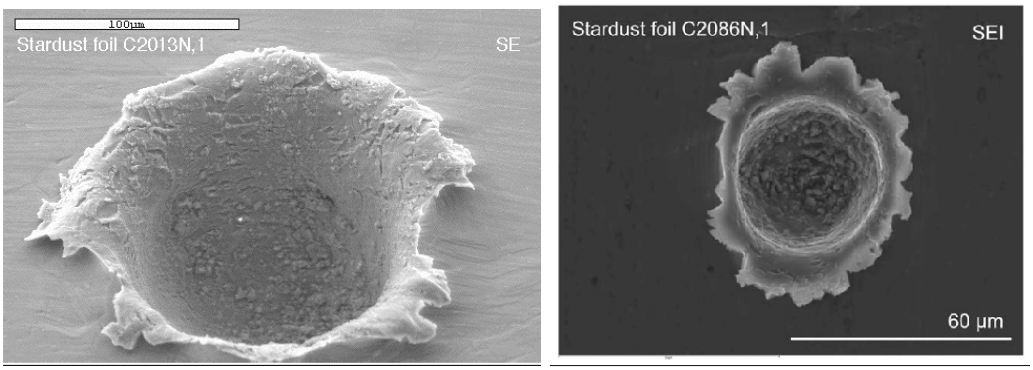

Figure 10: SEM images of large craters in Al foils C2013N and C2086N. The diameters of these craters are 140 µm and 59 µm, respectively.

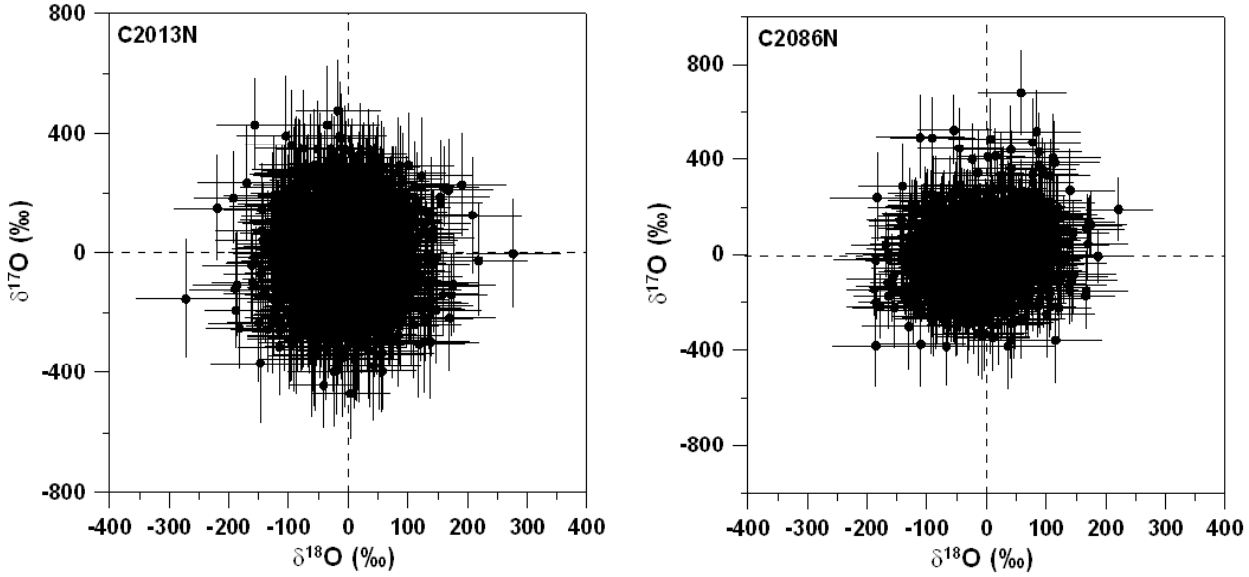

Figure 11: O isotopic compositions of O-rich particles (subareas) in crater C2013N (left) and C2086N (right). Only data from subareas with errors in $\delta^{17}O$ < 200 ‰ are shown. Error bars are 1σ.

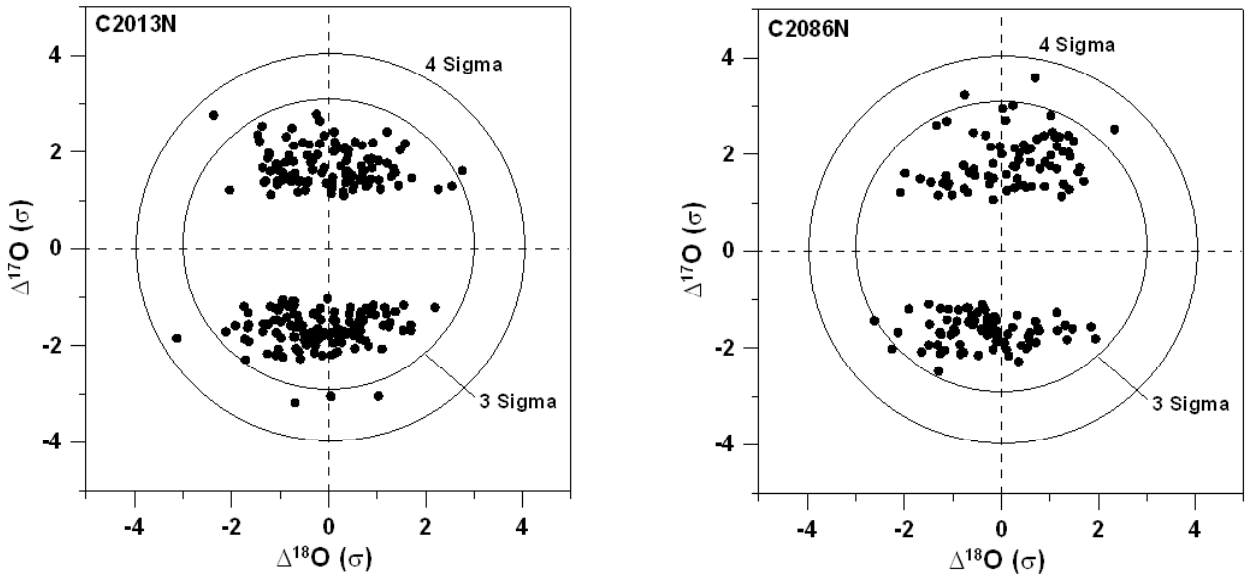

Figure 12: Sigma deviations of O isotopic ratios of O-rich particles (subareas) in crater C2013N (left) and C2086N (right). Only data of grains with $\delta^{17}O > +200$ ‰ and $\delta^{17}O < -200$ ‰ are shown. No grains plot outside the 4 σ limit.

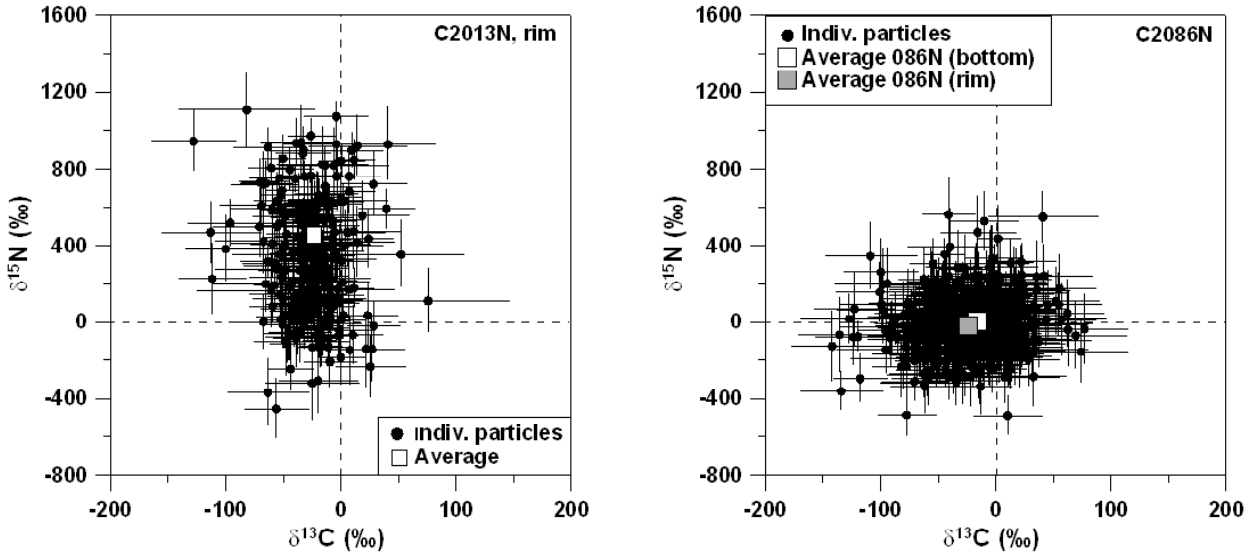

Figure 13: C and N isotopic compositions of individual N-rich particles/subareas and of their averages in craters C2013N (left) and C2086N (right). Errors are 1σ. Only data points with error of less than 200 ‰ in $\delta^{15}N$ and less than 50 ‰ in $\delta^{13}C$ are shown.

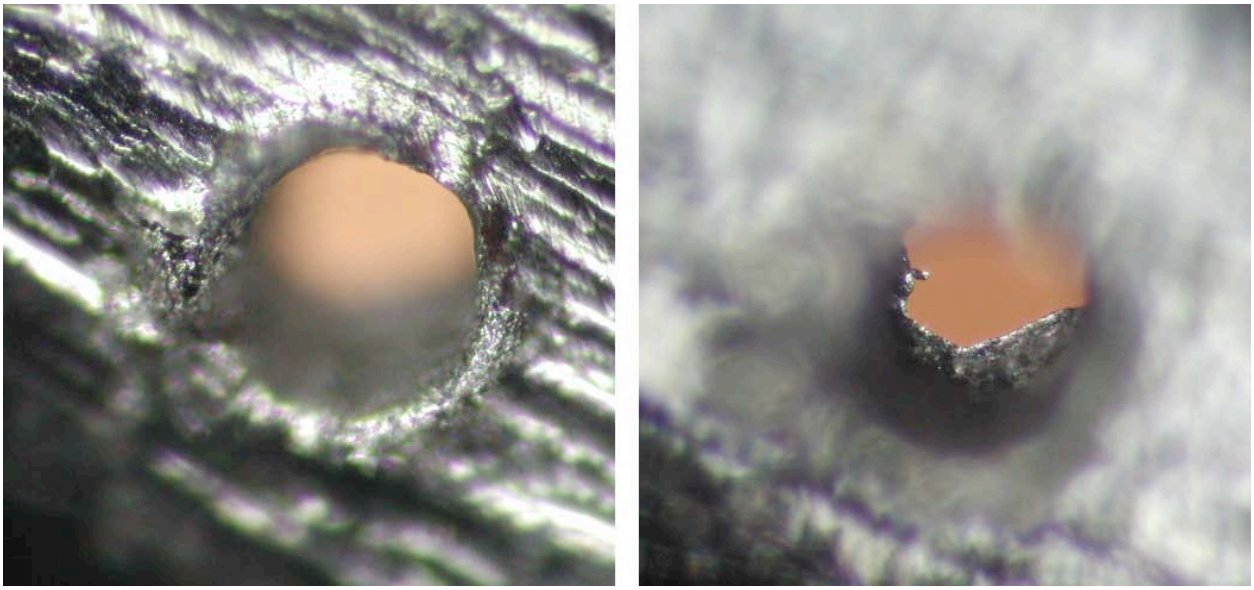

Figure 14: Optical images of the penetration crater C2086W with back illumination and different focal planes. The diameter of the crater is ~370 µm.

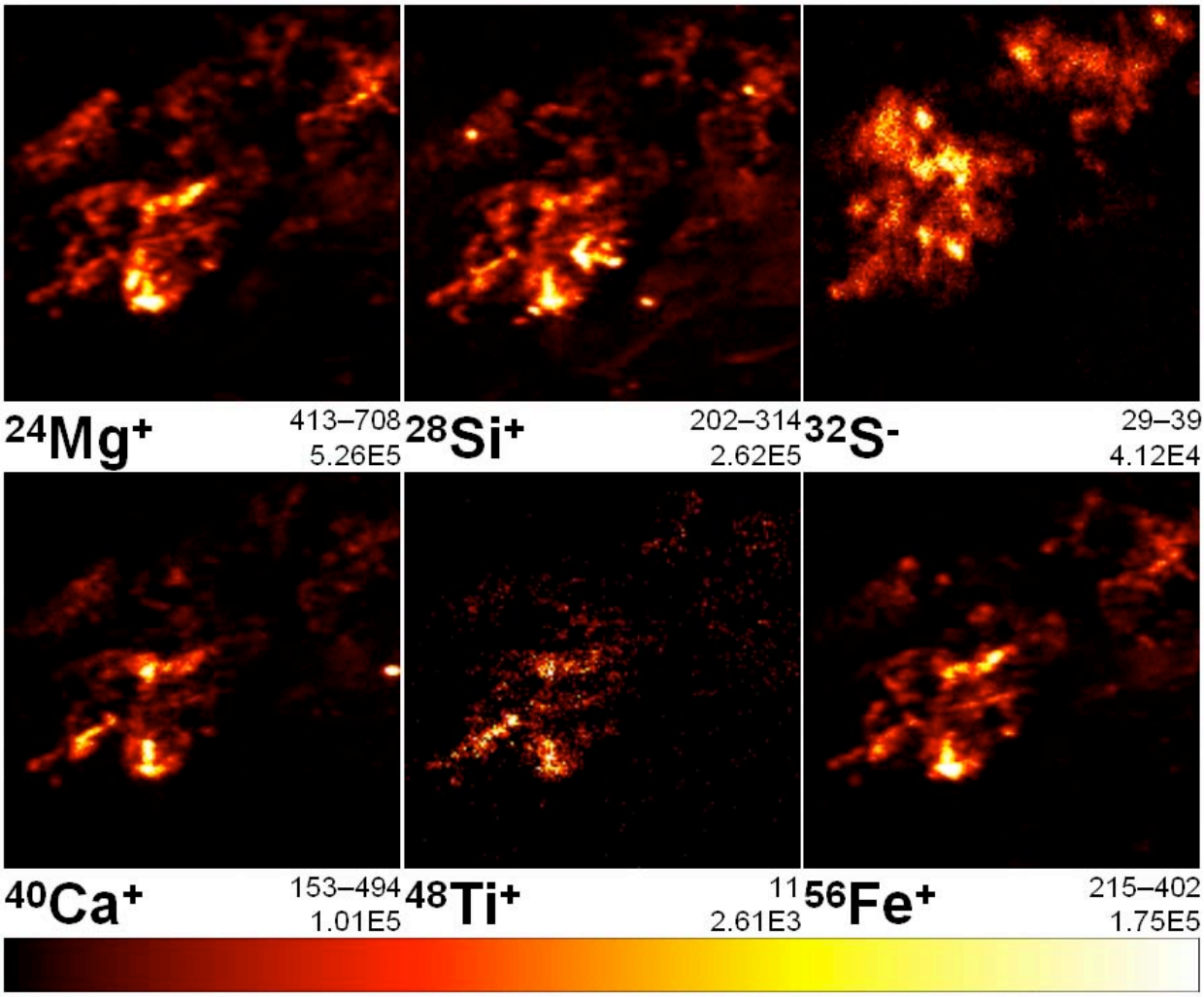

Figure 15: TOF-SIMS elemental distribution images on the rim of crater C2086W. The area shown is 50 x 50 μm^2. All individual ion images use the same linear color scale shown, where black always corresponds to zero counts and white is used for an intensity range given below every image (e.g., 413 – 708 counts for $^{24}Mg^+$). The other number underneath each image is the integrated intensity of the entire field of view (e.g., 5.26 x 10^5 counts for $^{24}Mg^+$).

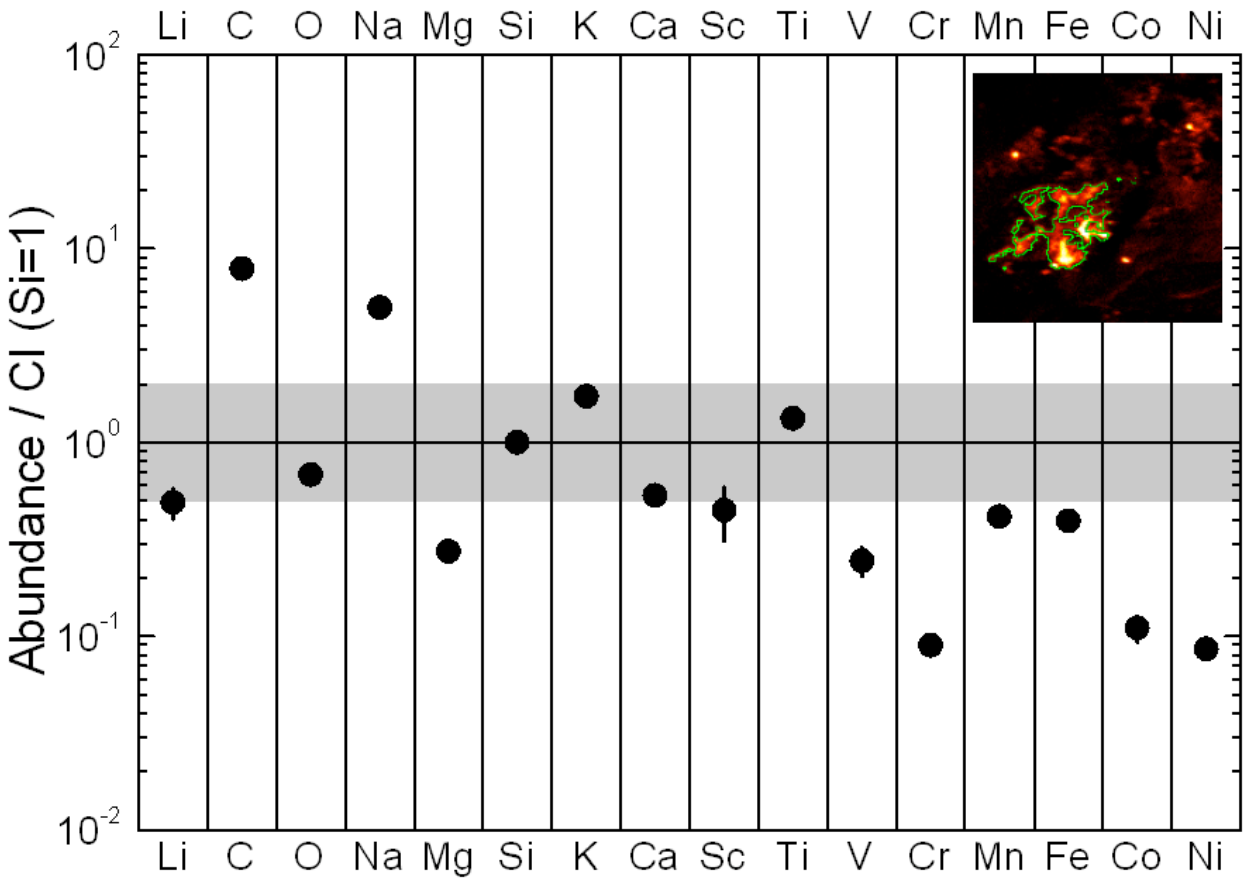

Figure 16: Element ratios relative to Si and normalized to CI chondrites of residual matter on the rim of crater C2086W measured by TOF-SIMS. These abundances represent the composition in the outlined area in the insert.

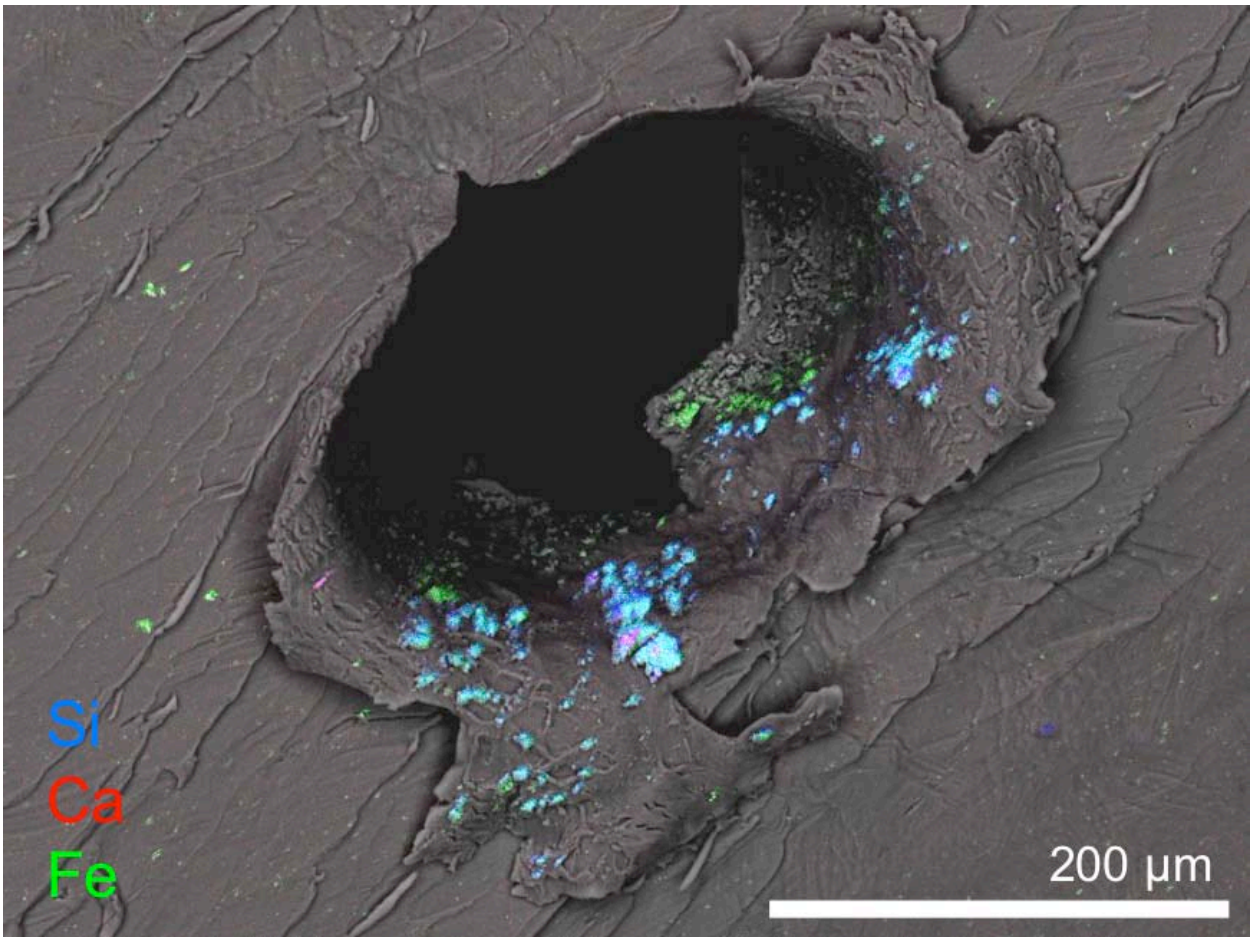

Figure 17: SEM image of the entire C2086W crater with an RGB overlay of EDX data. The distribution Si is shown in blue, Ca in red and Fe in green. The large Si-rich area in the center was subsequently analyzed by NanoSIMS.

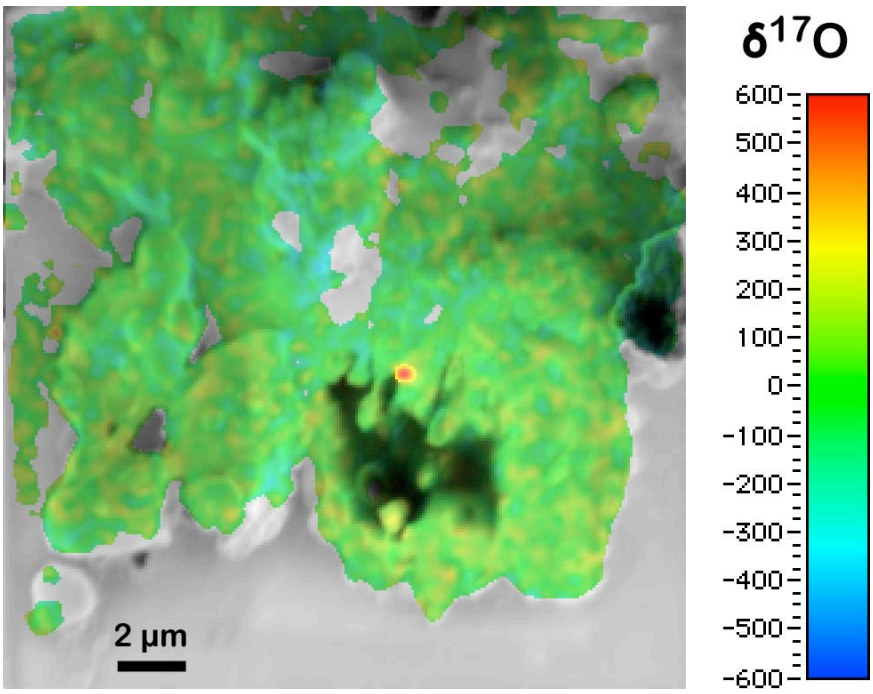

Figure 18: Composite NanoSIMS image of the area on the rim of crater C2086W where the presolar grain was found. The underlying grayscale image shows the morphology of the area as a secondary electron image. The overlay is a false color isotope ratio image of the distribution of $\delta^{17}O$ (in ‰) in the same location. Regions without colored overlay did not yield sufficient O for a meaningful isotope ratio determination. Most material is isotopically normal (i.e., $\delta^{17}O \approx 0$ ‰) and shown in green with some statistically insignificant variations. The red area in the center is the ^{17}O-rich presolar grain. More detailed follow-up measurements indicated that this grain is even more ^{17}O-rich than can be seen here.

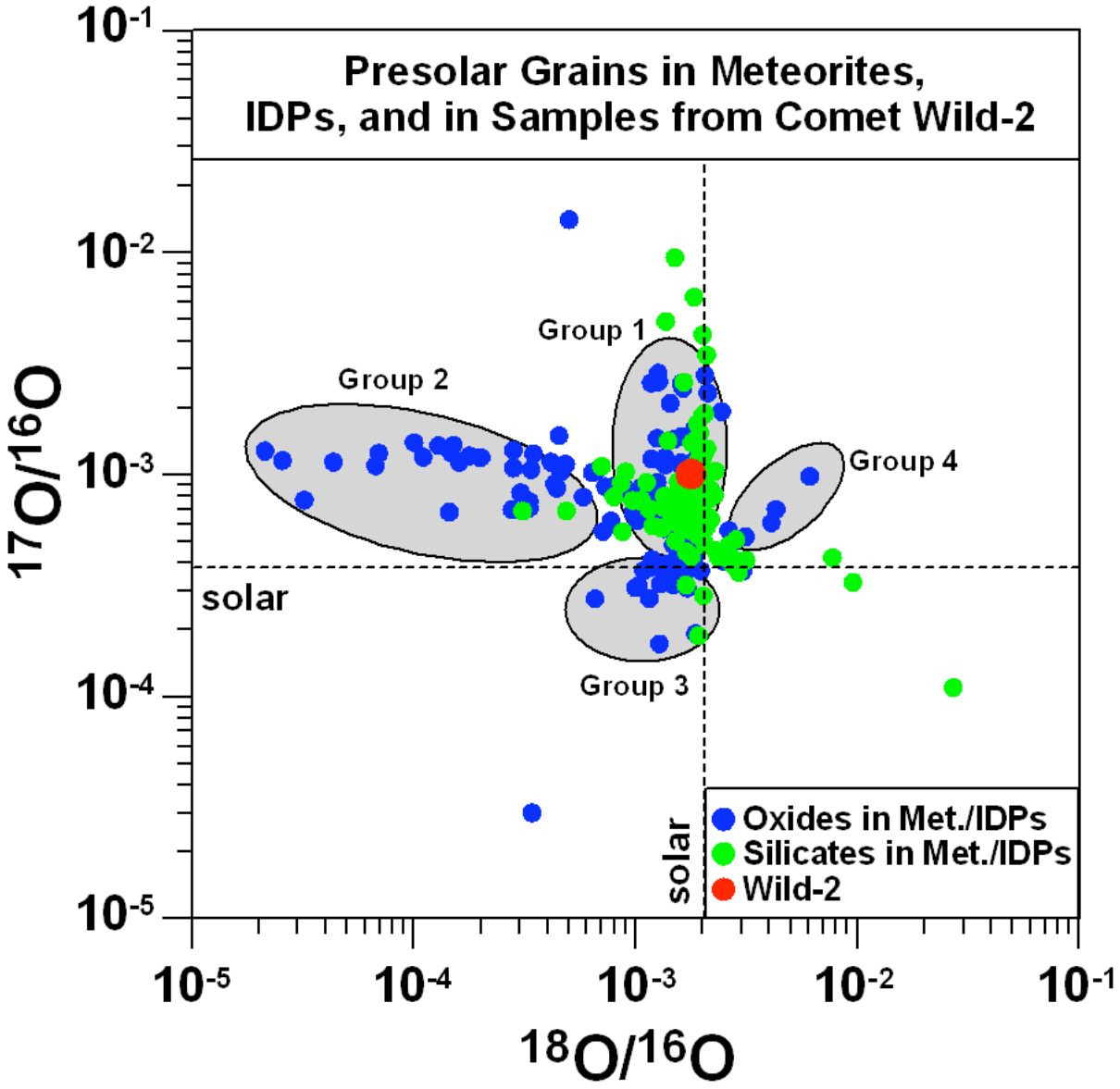

Figure 19: Oxygen three-isotope diagram with compositions of presolar oxide and silicate grains from primitive meteorites and from IDPs. The circumstellar grain from the Wild 2 cometary sample is shown in red with 1σ error bars smaller than the symbol. The areas for the different groups indicate different origins (Nittler et al. 1997). The oxide and silicate comparison data are from (Floss et al. 2006; Hoppe et al. 2005; Messenger et al. 2003a; 2005; Mostefaoui and Hoppe 2004; Nguyen and Zinner 2004; Nguyen et al. 2005; 2006; Nittler et al. 1994; 1997; 1998; Stadermann et al. 2005b; Zinner et al. 2005; Vollmer et al. 2007)